

AD-A045 668

SAINT LOUIS UNIV MO DEPT OF EARTH AND ATMOSPHERIC S--ETC F/G 8/11  
EARTHQUAKE GENERATED SH WAVES IN THE NEAR FIELD AND NEAR-REGION--ETC(U)  
AUG 77 R B HERRMANN

DACW39-76-C-0058

UNCLASSIFIED

WES-MP-S-77-12

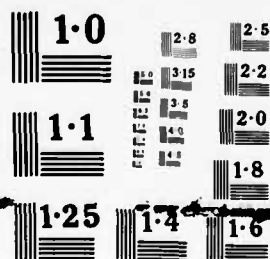
NL

1 OF 1  
ADA  
045668



END  
DATE  
FILMED  
11-77  
DDC

1 OF 1  
ADA  
045668



NATIONAL BUREAU OF STANDARDS  
MICROCOPY RESOLUTION TEST CHART

AD A 045668



*P*



*E*

MISCELLANEOUS PAPER S-77-12

# EARTHQUAKE GENERATED SH WAVES IN THE NEAR FIELD AND NEAR-REGIONAL FIELD

by

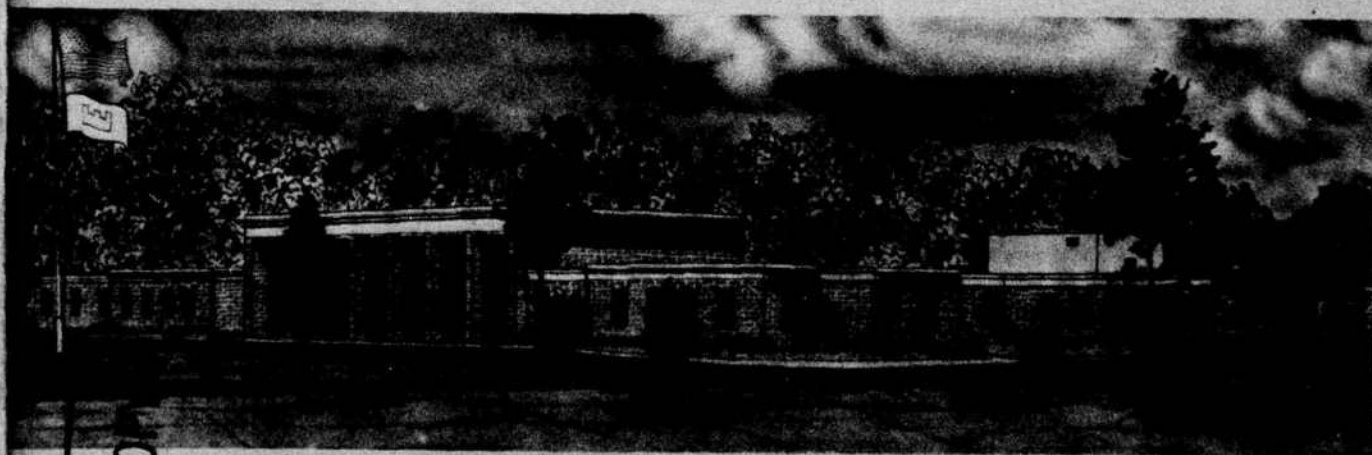
Robert B. Herrmann

St. Louis University  
Department of Earth and Atmospheric Sciences  
St. Louis, Missouri 63156

August 1977

Final Report

Approved For Public Release; Distribution Unlimited



AD NO. —  
DDC FILE COM

Prepared for Office, Chief of Engineers, U. S. Army  
Washington, D. C. 20314

Under Contract DACW 39-76-C-0058

Monitored by Soils and Pavements Laboratory  
U. S. Army Engineer Waterways Experiment Station  
P. O. Box 631, Vicksburg, Miss. 39180

DDC  
RECEIVED  
OCT 31 1977  
A

Destroy this report when no longer needed. Do not return  
it to the originator.



18 WES

Unclassified

SECURITY CLASSIFICATION OF THIS PAGE (When Data Entered)

REPORT DOCUMENTATION PAGE		READ INSTRUCTIONS BEFORE COMPLETING FORM
1. REPORT NUMBER Miscellaneous Paper S-77-12	2. GOVT ACCESSION NO.	3. RECIPIENT'S CATALOG NUMBER
4. TITLE (and Subtitle) Earthquake Generated SH Waves in the Near Field and Near-Regional Field	5. TYPE OF REPORT & PERIOD COVERED Final report	
7. AUTHOR(s) Robert B. Herrmann	8. CONTRACT OR GRANT NUMBER(s) DACW 39-76-C-0058	
9. PERFORMING ORGANIZATION NAME AND ADDRESS St. Louis University Department of Earth and Atmospheric Sciences St. Louis, Mo. 63156	10. PROGRAM ELEMENT, PROJECT, TASK AREA & WORK UNIT NUMBERS	
11. CONTROLLING OFFICE NAME AND ADDRESS Office, Chief of Engineers, U. S. Army Washington, D. C. 20314	12. REPORT DATE August 1977	
14. MONITORING AGENCY NAME & ADDRESS (if different from Controlling Office) U. S. Army Engineer Waterways Experiment Station Soils and Pavements Laboratory P. O. Box 631, Vicksburg, Miss. 39180	13. NUMBER OF PAGES 51	
16. DISTRIBUTION STATEMENT (of this Report) Approved for public release; distribution unlimited.		15. SECURITY CLASS. (of this report) Unclassified
17. DISTRIBUTION STATEMENT (of the abstract entered in Block 20, if different from Report)		
18. SUPPLEMENTARY NOTES		
19. KEY WORDS (Continue on reverse side if necessary and identify by block number) Earthquake prediction Ground motion predictions Seismic waves Shear waves Wave propagation		
20. ABSTRACT (Continue on reverse side if necessary and identify by block number) The prediction of earthquake strong motion values for aseismic design purposes is inhibited by scatter in previous correlations. Some of the scatter may be eliminated by a better understanding of the process of seismic wave transmission. This report is concerned with developing a methodology for predicting SH wave ground motion from earthquake sources in the distance range of 5-500 km for waves with frequencies less than 1.0 Hz. Suggestions for extending the methodology are also made.		

DD FORM 1 JAN 73 1473 EDITION OF 1 NOV 65 IS OBSOLETE

Unclassified

SECURITY CLASSIFICATION OF THIS PAGE (When Data Entered)

405292

JB

THE CONTENTS OF THIS REPORT ARE NOT TO BE  
USED FOR ADVERTISING, PUBLICATION, OR  
PROMOTIONAL PURPOSES. CITATION OF TRADE  
NAMES DOES NOT CONSTITUTE AN OFFICIAL EN-  
DORSEMENT OR APPROVAL OF THE USE OF SUCH  
COMMERCIAL PRODUCTS.

AMERICAN BIT	
White Section	<input checked="" type="checkbox"/>
Blue Section	<input type="checkbox"/>
Red Section	<input type="checkbox"/>
BY _____	
DATE _____	
APPROVED BY _____	
DATE _____	
A	

## PREFACE

This report was prepared by Dr. Robert B. Herrmann of St. Louis University, St. Louis, Missouri, as part of ongoing work at the U. S. Army Engineer Waterways Experiment Station (WES) in Civil Works Investigations, "Methodologies for Selecting Design Earthquakes," sponsored by the Office, Chief of Engineers, U. S. Army.

Preparation of the report was under the direction of Dr. Ellis L. Krinitzsky, Chief, Engineering Geology Research Facility, WES. General direction was by Mr. James P. Sale, Chief, Soils and Pavements Laboratory, and Mr. Don C. Banks, Chief, Engineering Geology and Rock Mechanics Division.

COL John L. Cannon, CE, was Commander and Director of WES; Mr. F. R. Brown was Technical Director.

# CONTENTS

	<u>Page</u>
PREFACE . . . . .	2
PART I: INTRODUCTION . . . . .	4
PART II: THEORY. . . . .	5
Statement of the Problem. . . . .	5
PART III: NUMERICAL TECHNIQUES AND TESTS . . . . .	12
Contour Integration . . . . .	12
Numerical Integration Techniques. . . . .	16
Independent Solution for Simplified Case. . . . .	19
Numerical Tests . . . . .	24
PART IV: SUMMARY AND CONCLUSIONS . . . . .	46
REFERENCES. . . . .	50
APPENDIX A: COMPUTER PROGRAM WESHASK . . . . .	A1
Function. . . . .	A1
Input . . . . .	A1
Output. . . . .	A1
File Codes. . . . .	A1
Sample Input. . . . .	A2
Program Listing . . . . .	A2
APPENDIX B: COMPUTER PROGRAM WESREFL . . . . .	B1
Function. . . . .	B1
Input . . . . .	B1
Output. . . . .	B1
Sample Input . . . . .	B1
Program Listing . . . . .	B1

NOTE: Appendixes A and B have been deleted to comply with  
ER 18-1-6.



EARTHQUAKE GENERATED SH WAVES IN THE NEAR FIELD  
AND NEAR-REGIONAL FIELD

PART I: INTRODUCTION

1. The description of earthquake generated ground motion is a difficult problem due to the complex nature of the earthquake process itself as well as the process of transmission of seismic energy through the real earth. Because of this complexity, it is difficult to fit observed earthquake strong motion data to simple prediction models with any reliability. Many attempts have been made to fit strong motion data as a function of parameters such as earthquake magnitude, focal depth and epicentral distance. Such models usually succeed in predicting the mean of the observed data set, but because of their strictly empirical nature offer no insight to the cause of the scatter.

2. Some of the error in the fit of these predictive models can be accounted for by making the model more complex. However, this cannot be done blindly since the addition of the extra parameters required to explain the scatter of simpler models may not have a theoretical justification. In any case, a model based upon a strictly empirical fit may not be general enough to admit additions to the data base. A better approach to the modeling of observed data is to perform a theoretical study of the generation of earthquake ground motion so that an insight on the choice of the empirical model used can be obtained.

3. The purpose of this report is to present work performed on modeling the SH component of ground motion for elementary earthquake point sources for ground motions with frequencies less than 1.0 Hz at observation sites 5-500 km from the source. While the extension of this report to include higher frequencies is important for the understanding of theoretical SH wave propagation in these distances ranges, the spatial inhomogeneities of the real earth are such that an analytical solution is not obtainable at frequencies much greater than 1 Hz for a real earth. However the insights of the modeling performed here will be of great value in understanding the gross properties of the high frequency content of earthquake generated motion.

## PART II: THEORY

4. A recent paper by HelMBERGER and Malone<sup>1</sup> demonstrates how well earthquake ground motion can be modeled by taking into account the effect of crustal layering on the seismic signal. They used a generalized ray technique<sup>2,3</sup> to construct their solution. This technique involves the computation of all possible contributions to the seismic signal, whether due to multiple reflection or refraction. The advantage of this technique is that it is valid for high frequencies. A disadvantage, though, is that for a reasonable model of the earth the number of individual ray contributions to the seismic signal becomes so large that the computer algorithm required is also very complex. The generalized ray technique is thus limited to either simple earth models or to studies of just part of the total ground motion time history.

5. Another approach is that developed by Haskell<sup>4</sup> and Hudson.<sup>5</sup> This method does not consider the contribution of the individual reflected and refracted arrivals, but rather yields the complete solution for a source in a layered halfspace. The drawback of the wave theory approach is the difficulty of finding solutions at high frequencies. However, the earth model can be as complicated as required. It is the wave theory method that is the subject of this report. The basic theory used is a modification of that developed by Haskell<sup>4</sup> and Hudson.<sup>5</sup> The modifications involved recasting their solutions into forms amenable to the numerical computation of not only the surface wave but also the refracted and reflected body wave contributions.

### Statement of the Problem

6. The problem considered is that of SH wave generation by an elementary point source in the  $m^{\text{th}}$  layer of an N layered structure with an upper free surface. Each layer is homogeneous and isotropic

with compressional wave velocity  $\alpha_k$ , shear wave velocity  $\beta_k$ , and density  $\rho_k$  ( $k = 1, N$ ). The  $N^{\text{th}}$  layer extends downwards to infinity. A cylindrical coordinate system  $(r, \phi, z)$  is used with origin on the free surface directly above the source, with the  $z$ -axis taken positive downwards. The layer interfaces are the planes  $z = z_k$  ( $k = 1, 2, \dots, N-1$ ). The source is situated on the plane  $z = z_{m-1} + h_m$ . For purposes of derivation, the source is restricted to lie in one of the layers above the halfspace.  $d_m = z_m - z_{m-1}$  is the thickness of the  $m^{\text{th}}$  layer.

7. Hudson<sup>5</sup> gives the following expression for the Fourier transform of the displacements at the free surface  $z = 0$ :

$$\begin{aligned}\bar{u}_r(r, \phi, \sigma, \omega) &= \sum_{n=0}^{\infty} \int_0^{\infty} dk \left\{ (g_r^{nc} \cos n\phi + g_r^{ns} \sin n\phi) \frac{\partial J_n(kr)}{\partial r} \cdot \frac{1}{F} \right. \\ &\quad \left. - \frac{n}{r} (g_\phi^{nc} \cos n\phi + g_\phi^{ns} \sin n\phi) J_n(kr) / F_L \right\} \\ \bar{u}_\phi(r, \phi, \sigma, \omega) &= \sum_{n=0}^{\infty} \int_0^{\infty} dk \left\{ \frac{n}{r} (g_r^{ns} \cos n\phi - g_r^{nc} \sin n\phi) J_n(kr) / F \right. \\ &\quad \left. - (g_\phi^{ns} \cos n\phi - g_\phi^{nc} \sin n\phi) \frac{\partial J_n(kr)}{\partial r} \cdot \frac{1}{F_L} \right\} \\ \bar{u}_z(r, \phi, \sigma, \omega) &= \sum_{n=0}^{\infty} \int_0^{\infty} dk \left\{ (g_z^{nc} \cos n\phi + g_z^{ns} \sin n\phi) J_n(kr) / F \right\}.\end{aligned}\tag{1}$$

In this expression  $\bar{u}_r$ , the radial displacement, is positive in a direction away from the source;  $\bar{u}_\phi$ , the tangential displacement, is positive in a direction of increasing  $\phi$ ;  $\bar{u}_z$ , the vertical displacement, is positive downward. The explicit expressions for the various terms in these equations are given by Haskell<sup>4</sup> and Hudson.<sup>5</sup>

8. Care must be taken in evaluating the expressions in Equation 1 because of the presence of non-causal terms.<sup>6</sup> The non-causality of certain parts of the solution arises because cylindrical potentials were used to form the solution, when a cartesian coordinate system would be more appropriate. Because of this, the nature of the solution of Equation 1 is such that very close to the source the tangential and radial displacements contain P, SV, and SH wave components.

9. The solution of Equation 1 is simplified if one is interested primarily in the propagating wave contribution. Using the relation

$$\frac{\partial}{\partial r} J_n(kr) = k J_{n-1}(kr) - \frac{n}{r} J_n(kr) \quad (2)$$

and ignoring terms decreasing faster than  $r^{-1}$ , the solution for the Fourier transform of the tangential displacements becomes

$$\bar{u}_\phi(r, \phi, 0, \omega) = \sum_{n=0}^{\infty} \int_0^{\infty} -(g_\phi^{ns} \cos n\phi - g_\phi^{nc} \sin n\phi) J_{n-1}(kr) F_L^{-1} k \, dk, \quad (3)$$

where

$$\begin{aligned} g_\phi^{nc} &= (L_{21} - L_{11}) s_1^{nc} + (L_{22} - L_{12}) s_2^{nc} \\ g_\phi^{ns} &= (L_{21} - L_{11}) s_1^{ns} + (L_{22} - L_{12}) s_2^{ns} \end{aligned} \quad (4)$$

$$F_L = J_{11} - J_{21}.$$

10. The  $L_{ij}$  and  $E_{ij}$  are elements of the  $L$  and  $E$  matrices which are defined by the matrix products

$$J = E_N^{-1} A_{N-1}(d_{N-1}) \dots A_1(d_1) \quad (5)$$

$$L = E_N^{-1} A_{N-1}(d_{N-1}) \dots A_{m+1}(d_{m+1}) D_m(d_m - h_m).$$

The various matrices in Equation 5 are defined as

$$E_N^{-1} = \begin{vmatrix} \rho_N \nu \beta_N & 0 \\ 0 & -1/\beta_N^2 \end{vmatrix} \quad (6)$$

$$A(z) = \begin{vmatrix} C_\beta & S_\beta / \rho \beta^2 v_\beta \\ \rho \beta^2 v_\beta S_\beta & C_\beta \end{vmatrix} \quad (7)$$

and

$$D(z) = \begin{vmatrix} C_\beta / \rho & -S_\beta / \rho v_\beta \\ \beta^2 v_\beta S_\beta & -\beta^2 C_\beta \end{vmatrix} \quad (8)$$

where  $C_\beta(z) = \cosh v_\beta z$ ,  $S_\beta(z) = \sinh v_\beta z$ , and

$$v_\beta = \begin{cases} (k^2 - k_\beta^2)^{1/2} & k > k_\beta \\ i(k_\beta^2 - k^2)^{1/2} & k \leq k_\beta \end{cases} .$$

The elements of the matrices are to be evaluated using the layer parameters of the particular indicated by the subscripts of Equation 5.

11. The source coefficients  $s_j^{nc,s}$  are adapted from Haskell.<sup>4</sup> It is generally accepted that a system of point forces oriented to form a double-couple without moment, or equivalently two perpendicular dipoles of opposite sign, is an adequate representation of the dislocation model of an earthquake source. Movement on a fault plane can be described by either of the two force systems mentioned above or by defining the direction of slip on a fault plane of given dip and strike. The interrelationship of these three ways of describing the earthquake source is given by Herrmann.<sup>7</sup> The use of the perpendicular dipole representation leads to the least confusion in application. Let the orientation of the tension and pressure axes in cartesian coordinates be given by the vectors  $\vec{F} = (f_1, f_2, f_3)$  and  $\vec{n} = (n_1, n_2, n_3)$ , respectively. The source coefficients  $s_i^{nc}$  and  $s_i^{ns}$  are all zero except for the terms

$$s_1^{lc} = -2(f_1 f_3 - n_1 n_3) / 4\pi \beta_m^2$$

$$\begin{aligned}
s_1^{1s} &= -2(f_2 f_3 - n_2 n_3)/4\pi\beta_m^2 \\
s_2^{2c} &= k(f_2^2 - f_1^2 - n_2^2 + n_1^2)/4\pi\beta_m^2 \\
s_2^{2s} &= -2k(f_1 f_2 - n_1 n_2)/4\pi\beta_m^2,
\end{aligned} \tag{9}$$

where  $k$  is the wavenumber and  $\beta_m$  is the shear wave velocity in the source layer. The expressions for  $E_N^{-1}$ ,  $D$ , and  $s_i^{nc,s}$  differ from those given by Haskell<sup>4</sup> and Hudson<sup>5</sup> in that they have been modified to eliminate apparent numerical singularities. The final solution given by Equation 3 is the same as that given by these authors.

12. For an earthquake source described by the source coefficients of Equation 9, the desired solution of Equation 3 can be rewritten as the sum of two terms:

$$\bar{u}_\phi(r, \phi, 0, \omega) = F_1(\bar{f}, \bar{n}, \phi)G_1 + F_2(\bar{f}, \bar{n}, \phi)G_2, \tag{10}$$

where

$$\begin{aligned}
G_1 &= \int_0^\infty -(g_1/F_L)J_0(kr)k \, dk \\
G_2 &= \int_0^\infty -(g_2/F_L)J_1(kr)k \, dk \\
g_1 &= L_{21} - L_{11} \\
g_2 &= k(L_{22} - L_{12}) \\
F_L &= J_{11} - J_{21} \\
F_1(\bar{f}, \bar{n}, \phi) &= -2[(f_2 f_3 - n_2 n_3)\cos\phi - (f_1 f_3 - n_1 n_3)\sin\phi]/4\pi\beta_m^2 \\
F_2(\bar{f}, \bar{n}, \phi) &= -[2(f_1 f_2 - n_1 n_2)\cos 2\phi + (f_2^2 - f_1^2 - n_2^2 + n_1^2)\sin 2\phi]/4\pi\beta_m^2.
\end{aligned} \tag{11}$$



13. To understand the source terms, three simple models of an earthquake are considered. Let the x and y axes of the cartesian coordinate system point north and east, respectively. The angle  $\phi$  is then the azimuth measured clockwise from north.

a. Right lateral vertical strike-slip fault striking north

$$\bar{f} = (-.707, .707, 0) \quad \bar{n} = (.707, .707, 0)$$

$$F_1(\bar{f}, \bar{n}, \phi) = 0$$

$$F_2(\bar{f}, \bar{n}, \phi) = 2 \cos 2\phi / 4\pi\beta_m^2$$

b. Thrust faulting on a fault dipping  $45^\circ$  to the east or west and striking north ( $45^\circ$  dip slip)

$$\bar{f} = (0, 0, 1) \quad \bar{n} = (0, 1, 0)$$

$$F_1(\bar{f}, \bar{n}, \phi) = 0$$

$$F_2(\bar{f}, \bar{n}, \phi) = \sin 2\phi / 4\pi\beta_m^2$$

c. Vertical dip slip faulting on a fault striking north with the east side downthrown

$$\bar{f} = (0, .707, .707) \quad \bar{n} = (0, -.707, .707)$$

$$F_1(\bar{f}, \bar{n}, \phi) = -2 \cos \phi / 4\pi\beta_m^2$$

$$F_2(\bar{f}, \bar{n}, \phi) = 0 .$$

14. An examination of these terms indicates that for vertical strike slip faulting or for  $45^\circ$  dip slip faulting, the solution for SH wave motion is proportional to the function  $G_2$  only. Likewise for pure dip slip on a vertical fault, the SH wave motion is a function of

$G_1$  only. It is also interesting to note that a vertical strike slip fault is twice as efficient a generator of SH waves as a  $45^\circ$  dip slip fault. The numerical techniques and examples to follow deal with the functions  $G_1$  and  $G_2$  only, and must be multiplied by  $F_1(\bar{f}, \bar{n}, \phi)$  and  $F_2(\bar{f}, \bar{n}, \phi)$  for proper scaling before the synthetic seismograms are compared to real data.

15. After Equation 10 is evaluated, it must be multiplied by the Fourier transform  $S(\omega)$  of  $s(t)$ , the source time function. For a dislocation source,  $s(t)$  represents the time history of the faulting process for which  $s(t) = 0$  for  $t < 0$  and  $s(t) = M_0$  for  $t \gg 0$ . The seismic moment  $M_0$  is defined by the relation  $M_0 = \mu \bar{u} A$ , where  $\mu$  is the rigidity of the medium in which the faulting occurs,  $\bar{u}$  is the average fault displacement and  $A$  is the fault area. In normal use the CGS units of  $M_0$  are dyne-cm. The SH wave ground motion as a function of time is obtained by taking the inverse Fourier transform of the product of  $S(\omega)$  and Equation 3:

$$u_\phi(r, \phi, 0, t) = (2\pi)^{-1} \int_{-\infty}^{\infty} S(\omega) \bar{u}_\phi(r, \phi, 0, \omega) \exp(i\omega t) d\omega. \quad (12)$$

Hudson<sup>5</sup> discusses the mathematics of superposition of solutions such as Equation 12 to represent extended sources and complex rupturing processes. However, these extensions are beyond the scope of this report.

### PART III: NUMERICAL TECHNIQUES AND TESTS

16. As seen in the previous section, the solution of SH wave motion due to an arbitrary point dislocation source model of an earthquake reduced to the evaluation of two integrals,

$$\begin{aligned} G_1 &= \int_0^{\infty} -(g_1/F_L) J_0(kr) k \, dk \\ G_2 &= \int_0^{\infty} -(g_2/F_L) J_1(kr) k \, dk \end{aligned} \quad (13)$$

where  $g_1$ ,  $g_2$ , and  $F_L$  are defined in Equation 11. The objective of this section is to recast these integrals into a form suitable for numerical integration. As an independent test of the numerical integration technique, the problem is solved by a different technique for a simple earth model, and the two solutions are compared.

#### Contour Integration

17. A contour integration method for evaluation of integrals of the form of Equation 13 has been described by many authors. The development given here parallels one presented by Ewing, Jardetzky and Press.<sup>8</sup>

18. The two integrals in Equation 13 are of the general form

$$I = \int_0^{\infty} f(k, \omega) J_n(kr) k \, dk \quad (14)$$

The function  $f(k, \omega)$  has a finite number of poles on the real axis for  $k_{\beta_N} \leq k \leq k_{\beta_1}$  and a branch point at  $k = k_{\beta_N}$ . From Equation 13,

$f(k, \omega) = g_1/F_L$  for  $n = 0$  and  $f(k, \omega) = g_2/F_L$  for  $n = 1$ . A study of the functional forms of  $g_1$ ,  $g_2$ , and  $F_L$  shows that  $f(k, \omega)$  is even in  $k$  for  $n$  even and odd in  $k$  for  $n$  odd.

19. The Bessel function of the first kind can be expressed in

terms of the Hankel functions of the first and second kind by the relation

$$J_n(kr) = \frac{1}{2} [ H_n^{(1)}(kr) + H_n^{(2)}(kr) ] . \quad (15)$$

Using Equations 14 and 15, one obtains

$$\begin{aligned} I &= \frac{1}{2} \int_0^{\infty} f(k, \omega) H_n^{(1)}(kr) k \, dk \\ &\quad + \frac{1}{2} \int_0^{\infty} f(k, \omega) H_n^{(2)}(kr) k \, dk \\ &= I_1 + I_2 . \end{aligned} \quad (16)$$

20. The integrals of Equation 16 are improper since the integrands become infinite at the zeros of  $F_L$ . To evaluate these integrals, contour integration is performed in the complex  $k$  plane. The contours for evaluating  $I_1$  and  $I_2$  are shown in Figures 1a and 1b, respectively.<sup>5,8</sup>

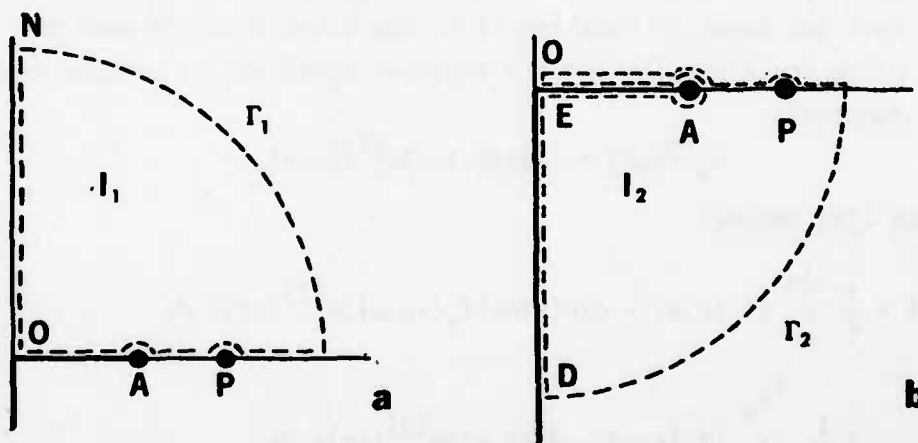


Fig 1. Contours in complex  $k$  plane for evaluating the integrals  $I_1$  and  $I_2$

In these figures,  $A$  is the branch point,  $P$  is a pole on the real axis, and the heavy line along part of the real axis and along the negative imaginary axis is the branch cut. These contours are chosen since

$H_n^{(1)}(kr)$  is analytic in the first quadrant while  $H_n^{(2)}(kr)$  is analytic in the fourth quadrant of the complex  $k$  plane. In the first quadrant,  $\text{Im } \nu_{\beta_N} \geq 0$  and  $\text{Re } \nu_{\beta_N} \geq 0$ , while in the fourth quadrant  $\text{Im } \nu_{\beta_N} \leq 0$  and  $\text{Re } \nu_{\beta_N} \geq 0$ .

21. Using Cauchy's integral theorem, Equation 16 becomes

$$\begin{aligned}
 I = & \frac{1}{2} \int_0^N f(\zeta, \omega) H_n^{(1)}(\zeta r) \zeta d\zeta + \frac{1}{2} \int_E^D f(\zeta, \omega) H_n^{(2)}(\zeta r) \zeta d\zeta \\
 & + \frac{1}{2} \int_{OAE} f(\zeta, \omega) H_n^{(2)}(\zeta r) \zeta d\zeta - \pi i \sum \text{Res}[f(\zeta, \omega) H_n^{(2)}(\zeta r) \zeta] \quad (17) \\
 & + \frac{1}{2} \int_{\Gamma_1} f(\zeta, \omega) H_n^{(1)}(\zeta r) \zeta d\zeta + \frac{1}{2} \int_{\Gamma_2} f(\zeta, \omega) H_n^{(2)}(\zeta r) \zeta d\zeta .
 \end{aligned}$$

As the arcs  $\Gamma_1$  and  $\Gamma_2$  extend outward to infinity, the contribution of the last two terms in Equation 17 to the total solution goes to zero. Using an expression for the analytic continuation between the Hankel functions

$$H_n^{(1)}(\zeta r) = -\exp(-in\pi) H_n^{(2)}(-\zeta r),$$

Equation (17) becomes

$$\begin{aligned}
 I = & \frac{1}{2} \int_0^{-i\infty} [f_-(\zeta, \omega) - \exp(-in\pi) f_+(-\zeta, \omega)] H_n^{(2)}(\zeta r) \zeta d\zeta \\
 & + \frac{1}{2} \int_0^{k_{\beta_N}} [f_+(k, \omega) - f_-(k, \omega)] H_n^{(2)}(kr) k dk \quad (18) \\
 & - \pi i \sum \text{Res}[f(\zeta, \omega) H_n^{(2)}(\zeta r) \zeta] ,
 \end{aligned}$$

where the + or - subscripts indicate that  $\text{Im } \nu_{\beta_N} > 0$  or  $\text{Im } \nu_{\beta_N} < 0$ , respectively, is to be used to evaluate the expressions for  $f(\zeta, \omega)$ .

22. By a simple change in variable Equation (18) can be rewritten as

$$\begin{aligned}
 I = & -\frac{1}{2} \int_0^{\infty} [f_-(-i\tau, \omega) - \exp(-in\pi) f_+(i\tau, \omega)] H_n^{(2)}(-i\tau) \tau \, d\tau \\
 & + \frac{1}{2} \int_0^{k_{\beta N}} [f_+(k, \omega) - f_-(k, \omega)] H_n^{(2)}(kr) k \, dk \\
 & - \pi i \left[ \text{Res}[f(\zeta, \omega) H_n^{(2)}(\zeta r) \zeta] \right].
 \end{aligned} \tag{19}$$

23. The final steps of the derivation make use of specific properties of the functions  $g_1$ ,  $g_2$ , and  $F_L$ . Letting  $f^1(\zeta, \omega) = g_1/F_L$  and  $f^2(\zeta, \omega) = g_2/F_L$ , it can be shown that

$$\begin{aligned}
 f_{+}^1(x, \omega) &= f_{+}^1(-x, \omega) \\
 f_{+}^2(x, \omega) &= -f_{+}^2(-x, \omega) \\
 f_{-}^1(-ix, \omega) &= \overline{f_{+}^1(ix, \omega)} \\
 f_{-}^2(-ix, \omega) &= \overline{f_{+}^2(ix, \omega)} \\
 f_{+}^{1,2}(x, \omega) &= \overline{f_{-}^{1,2}(x, \omega)},
 \end{aligned} \tag{20}$$

where  $x$  is a real quantity and the bar above the function indicates that the complex conjugate should be taken.



24. The modified expressions for  $G_1$  and  $G_2$  of Equation 13 finally become

$$G_1 = i \int_0^{k_{\beta N}} \text{Im}[f_+^1(k, \omega)] H_0^{(2)}(kr) k \, dk$$

$$- \pi i \sum \text{Res}[f_+^1(\zeta, \omega) H_0^{(2)}(\zeta r) \zeta] \quad (21a)$$

$$- \frac{2}{\pi} \int_0^{\infty} \text{Im}[f_+^1(i\tau, \omega)] K_0(\tau r) \tau \, d\tau$$

$$G_2 = i \int_0^{k_{\beta N}} \text{Im}[f_+^2(k, \omega)] H_1^{(2)}(kr) k \, dk$$

$$- \pi i \sum \text{Res}[f_+^2(\zeta, \omega) H_1^{(2)}(\zeta r) \zeta] \quad (21b)$$

$$+ \frac{2}{\pi} \int_0^{\infty} \text{Re}[f_+^2(i\tau, \omega)] K_1(\tau r) \tau \, d\tau \quad ,$$

where the additional relations

$$H_0^{(2)}(-iz) = -\frac{2}{i\pi} K_0(z)$$

and

$$H_1^{(2)}(-iz) = \frac{2}{\pi} K_1(z)$$

have been used.  $K_n(z)$  is a modified Bessel function of order  $n$ .

#### Numerical Integration Techniques

25. A computer program, WESHASK, has been written to perform the computations required to evaluate Equation 21. Appendix A contains a

listing and a description of the use of this program. It is appropriate to discuss the numerical integration techniques used as well as their limitations. Each of the three terms making up  $G_1$  and  $G_2$  in Equation 21 is discussed separately.

26. The first term in both  $G_1$  and  $G_2$  is an integral along the real axis of the form

$$\int_0^{k_{\beta_N}} f(k, \omega) H_n^{(2)}(kr) k dk \quad . \quad (22)$$

To evaluate this integral, a change of variable is introduced. Using relation  $k = k_{\beta_N} \sin \gamma$ , Equation 22 becomes

$$\int_0^{\pi/2} f(k_{\beta_N} \sin \gamma, \omega) H_n^{(2)}(k_{\beta_N} r \sin \gamma) k_{\beta_N}^2 \sin \gamma \cos \gamma d\gamma \quad . \quad (23)$$

The advantage of Equation 23 is that the integrand has a zero weight at  $k = k_{\beta_N}$ , where the branch point may introduce a singularity at some frequencies, as well as at  $k = 0$ , where the Hankel function becomes undefined.

27. Equation 23 is evaluated by using a trapezoidal integration rule:

$$\sum_{i=1}^{M-1} f(k_i, \omega) H_n^{(2)}(k_i r) k_{\beta_N}^2 \sin \gamma_i \cos \gamma_i \Delta \gamma \quad , \quad (24)$$

where

$$\Delta \gamma = \pi/2M \quad , \quad \gamma_i = i\Delta \gamma \quad , \quad \text{and } k_i = k_{\beta_N} \sin \gamma_i \quad .$$

28. The choice on the summation index  $M$  depends upon both the maximum angular frequency,  $\omega$ , and epicentral distance,  $r$ , considered. The Hankel function  $H_n^{(2)}(z)$  is an oscillatory function. To avoid numerical integration problems, the Hankel function must be sampled at least twice per oscillation. For a given frequency  $f$  ( $\omega = 2\pi f$ ) and distance  $r$ , the value of  $M$  should be large enough to

to approximate the inequality

$$M > \pi f r / \beta_N .$$

Good numerical results have been obtained using  $M = 100$  for frequencies less than 0.5 Hz for distances less than 500 km with  $\beta_N = 4.67$  km/sec. Even though this value of  $M$  does not satisfy the inequality, it is reasonable to expect that the guidance given by the above inequality yields the proper order of magnitude for  $M$ .

29. The second term for the expressions of  $G_1$  and  $G_2$  in Equation 21 is the residue contribution of the poles. For an earth model with no anelastic attenuation loss, the poles lie on the real axis in the range  $k_{\beta_N} \leq k \leq k_{\beta_1}$ . The poles are found by locating the zeros of the function  $F_L$  by a search in the region  $k_{\beta_N} + \Delta k \leq k \leq k_{\beta_1}$  to find zero crossings of the function, after which an interval halving process is used to refine the root. To avoid numerical problems at the branch point, a possible pole at  $k = k_{\beta_N}$  is neglected. This is a minor error if  $\Delta k$  is small enough. A value  $\Delta k = (k_{\beta_1} - k_{\beta_N})/100$  is used in the program. For reasonable continental crustal models with crustal thicknesses of about 40 km, this choice of  $\Delta k$  should be adequate to frequencies of 3 Hz, since the number of poles increases with increasing frequency. The residue contribution of a function  $g(z)/h(z)$ , having a zero of  $h(z)$  at  $z = z_0$ , is very simply

$$g(z_0)/h'(z_0),$$

where  $h'(z)$  is the first derivative of  $h(z)$ .

30. The third term in the expressions for  $G_1$  and  $G_2$  is an integral of the form

$$\int_0^{\infty} f(i\tau, \omega) K_n(\tau r) \tau d\tau, \quad (25)$$

where  $f(i\tau, \omega)$  is a complex quantity. The function  $K_n(z)$  decreases in an exponential manner for increasing  $z$  and has a singularity at  $z = 0$ . The exponential decrease with large values of the argument suggests the

use of a Gauss-Laguerre integration rule if  $f(i\tau, \omega)$  does not oscillate too fast. After a change of variable and application of the Gauss-Laguerre integration rule, Equation 25 is approximated by

$$\frac{1}{r^2} \sum_{k=1}^m w_k \left[ f\left(\frac{ix_k}{r}, \omega\right) x_k \exp(x_k) K_n(x_k) \right] \quad (26)$$

where  $x_k$  and  $w_k$  are the abscissas and weights of an  $m^{\text{th}}$  order Gauss-Laguerre rule.

31. Error is introduced into the evaluation of Equation 26 because of the oscillatory nature of  $f(i\tau, \omega)$ . This can be mitigated by using a very high order rule, so that the abscissas are closely enough spaced. Because the weights  $w_k$  decrease very fast for large values of the index  $k$ , one does not need to use all  $m$  terms of the summation. The computer program WESHASK uses the first 24 weights and abscissas of a  $m = 68$  order rule which were taken from the tables of Stroud and Secrest.<sup>9</sup> Because of the  $r^{-2}$  term in the expression, the contribution of Equation 26 to the total solution only becomes important at short distances. The approximation used in the computer program gives good results for distances greater than 5 km and for frequencies less than 1 Hz.

#### Independent Solution for Simplified Case

32. To test the computer program WESHASK, an independent solution was found for the simple case of a source within a single layer overlying a halfspace. For a source at a depth  $h$  within a layer with thickness  $d_1$ , the expressions for  $G_1$  and  $G_2$  of Equation 11 take the form

$$G_1 = \int_0^\infty \frac{\frac{\beta_1^2}{\beta_2^2} v_{\beta_1} S'_{\beta_1} + \frac{\rho_2}{\rho_1} v_{\beta_2} C'_{\beta_1}}{\rho_2 v_{\beta_2} C_{\beta_1} + \rho_1 \frac{\beta_1^2}{\beta_2^2} v_{\beta_1} S_{\beta_1}} k J_0(kr) dk \quad (27a)$$

$$G_2 = \int_0^\infty \frac{\frac{\beta_1^2}{\beta_2^2} C_{\beta_1}' + \frac{\rho_2 v_{\beta_2}}{\rho_1 v_{\beta_1}} S_{\beta_1}'}{\rho_2 v_{\beta_2} C_{\beta_1} + \rho_1 \frac{\beta_1^2}{\beta_2^2} v_{\beta_1} S_{\beta_1}} k^2 J_1(kr) dk, \quad (27b)$$

where  $S_{\beta_1}' = S_{\beta_1}(d_1 - h_1)$ ,  $C_{\beta_1}' = C_{\beta_1}(d_1 - h_1)$ ,  $S_{\beta_1} = S_{\beta_1}(d_1)$  and  $C_{\beta_1} = C_{\beta_1}(d_1)$ . The other symbols are as previously defined.

33. Defining the layer rigidity as  $\mu_n = \rho_n \beta_n^2$  and a complex reflection coefficient as

$$R = \frac{\mu_2 v_{\beta_2} - \mu_1 v_{\beta_1}}{\mu_2 v_{\beta_2} + \mu_1 v_{\beta_1}},$$

Equation 27 can be rewritten as an infinite series as follows:

$$G_1 = \int_0^\infty \frac{1}{\rho_1} \left\{ \exp(-v_{\beta_1} h) + R \exp[-v_{\beta_1} (2d_1 - h)] - R \exp[-v_{\beta_1} (2d_1 + h)] \right. \\ \left. - R^2 \exp[-v_{\beta_1} (4d_1 - h)] + R^2 \exp[-v_{\beta_1} (4d_1 + h)] + \dots \right\} \quad (28)$$

$$G_2 = \int_0^\infty \frac{-k}{\rho_1 v_{\beta_1}} \left\{ \exp[-v_{\beta_1} h] - R \exp[-v_{\beta_1} (2d_1 - h)] \right. \\ \left. - R \exp[-v_{\beta_1} (2d_1 + h)] + R^2 \exp[-v_{\beta_1} (4d_1 - h)] \right. \\ \left. + R^2 \exp[-v_{\beta_1} (4d_1 + h)] + \dots \right\}.$$

34. This expansion is termed a generalized ray expansion since each term represents the contribution of rays that are multiply reflected after leaving the source. The first term in the  $G_1$  and  $G_2$  expansions represent the contribution of the direct ray from the source to the receiver at the free surface, while the next two terms represent rays that are reflected or refracted once from the interface at a depth  $z = d_1$ .<sup>8</sup> The term generalized ray is used since the integral of each term yields both the reflected and refracted arrivals associated with each ray. In an infinite medium, just the first term comprises the solution for  $G_1$  and  $G_2$  since  $R = 0$ .

35. The first terms of the expressions for  $G_1$  and  $G_2$  in Equation 28 can be evaluated directly by taking derivatives of the Sommerfeld integral. It can be easily shown that

$$\int_0^{\infty} \exp[-v_{\beta} h] J_0(kr) k \, dk = \frac{h}{R} \left( \frac{i\omega}{\beta R} + \frac{1}{R^2} \right) \exp(-ik_{\beta} R) = H_1 \quad (29)$$

$$\int_0^{\infty} \frac{k}{v_{\beta}} \exp[-v_{\beta} h] J_1(kr) k \, dk = \frac{r}{R} \left( \frac{i\omega}{\beta R} + \frac{1}{R^2} \right) \exp(-ik_{\beta} R) = H_2 ,$$

where  $R^2 = h^2 + r^2$ .

36. Equation 29 can be used to evaluate the individual terms of Equation 28. The two basic integrals to be evaluated are of the form

$$\int_0^{\infty} R^n \exp[-v_{\beta_1} Z] J_0(kr) k \, dk \quad (30a)$$

and

$$\int_0^{\infty} \frac{k}{v_{\beta_1}} R^n \exp[-v_{\beta_1} Z] J_1(kr) k \, dk . \quad (30b)$$

The evaluation of these two integrals is complicated by the oscillatory character of the Bessel function for large  $k$ . However, for large  $k$ , the complex reflection coefficient  $R$  approaches a limit,

$$R(\infty, \omega) = \frac{\mu_2 - \mu_1}{\mu_2 + \mu_1} . \quad (31)$$



37. The oscillatory behavior for large  $k$  can have a minimal effect if the integrals of Equation 30 are rewritten using Equations 29 and 31 in the following manner:

$$\int_0^{\infty} [R^n(k, \omega) - R^n(\infty, \omega)] \exp[-v_{\beta_1} Z] J_0(kr) k \, dk + R^n(\infty, \omega) H_1 \quad (32a)$$

$$\int_0^{\infty} \frac{k}{v_{\beta_1}} [R^n(k, \omega) - R^n(\infty, \omega)] \exp[-v_{\beta_1} Z] J_1(kr) k \, dk + R^n(\infty, \omega) H_2 . \quad (32b)$$

38. The integrals to be evaluated in Equation 32 are of the form

$$I_1 = \int_0^{\infty} g(k) \exp[-v_{\beta_1} Z] J_0(kr) k \, dk \quad (33a)$$

and

$$I_2 = \int_0^{\infty} \frac{k}{v_{\beta_1}} g(k) \exp[-v_{\beta_1} Z] J_1(kr) k \, dk, \quad (33b)$$

where  $g(k)$  is function which goes to zero for large  $k$ .

39. A critical point in the evaluation of Equation 33 is at  $k = k_{\beta_1}$ , where  $v_{\beta_1}$  changes from positive imaginary to positive real with increasing  $k$ . To properly take into account the change in character of the integrands, the integration is performed over two ranges by using the following transformations:

$$\underline{a.} \quad 0 \leq k \leq k_{\beta_1}$$

$$k = k_{\beta_1} \sin \gamma$$

$$dk = k_{\beta_1} \cos \gamma \, d\gamma$$

$$v_{\beta_1} = ik_{\beta_1} \cos \gamma, \quad \text{for } 0 \leq \gamma \leq \pi/2$$

$$\underline{b.} \quad k_{\beta_1} \leq k < \infty$$

$$k = k_{\beta_1} \cosh \eta$$

$$dk = k_{\beta_1} \sinh \eta \, d\eta$$

$$v_{\beta_1} = k_{\beta_1} \sinh \eta, \text{ for } 0 \leq \eta < \infty.$$

40. Using these transformations, Equations 33a and 33b become the following:

$$I_1 = \int_0^{\pi/2} g(k_{\beta_1} \sin \gamma) \exp[-ik_{\beta_1} Z \cos \gamma] J_0(k_{\beta_1} r \sin \gamma) k_{\beta_1}^2 \cos \gamma \sin \gamma \, d\gamma \\ + \int_0^{\infty} g(k_{\beta_1} \cosh \eta) \exp[-k_{\beta_1} Z \sinh \eta] J_0(k_{\beta_1} r \cosh \eta) k_{\beta_1}^2 \cosh \eta \sinh \eta \, d\eta \quad (34a)$$

$$I_2 = -i \int_0^{\pi/2} g(k_{\beta_1} \sin \gamma) \exp[-ik_{\beta_1} Z \cos \gamma] J_1(k_{\beta_1} r \sin \gamma) k_{\beta_1}^2 \sin^2 \gamma \, d\gamma \\ + \int_0^{\infty} g(k_{\beta_1} \cosh \eta) \exp[-k_{\beta_1} Z \sinh \eta] J_1(k_{\beta_1} r \cosh \eta) k_{\beta_1}^2 \cosh^2 \eta \, d\eta \quad (34b)$$

41. The first integral in the expressions for  $I_1$  and  $I_2$  is easily evaluated using a trapezoidal rule. The limitations on the applicability of the trapezoidal rule are as discussed previously in Paragraph 28. The second integral in each expression can be evaluated using the Gauss-Laguerre integration rule after one last transformation. Let  $x = k_{\beta_1} Z \sinh \eta$ . Then

$$dx = k_{\beta_1} Z \cosh \eta \, d\eta$$

and

$$[k_{\beta_1}^2 + (x/Z)^2]^{1/2} = k_{\beta_1} \cosh \eta.$$

42. The numerical approximations to  $I_1$  and  $I_2$  are finally

$$I_1 = \sum_{m=1}^{M-1} g[k(\gamma_m)] \exp[-ik_{\beta_1} Z \cos \gamma_m] J_0[k(\gamma_m) r] k_{\beta_1}^2 \sin \gamma_m \cos \gamma_m \, \Delta \gamma \\ + \frac{1}{Z^2} \sum_{j=1}^n w_j g[k(x_j)] x_j J_0[k(x_j) r] \quad (35a)$$

$$I_2 = -i \sum_{m=1}^{M-1} g[k(\gamma_m)] \exp[-ik_{\beta_1} Z \cos \gamma_m] J_1[k(\gamma_m)r] k_{\beta_1}^2 \sin^2 \gamma_m \Delta\gamma$$

$$+ \frac{1}{Z} \sum_{j=1}^n w_j g[k(x_j)] k(x_j) J_1[k(x_j)r] , \quad (35b)$$

where

$$\Delta\gamma = \pi/2M$$

$$\gamma_m = m \Delta\gamma$$

$$k(\gamma_m) = k_{\beta_1} \sin \gamma_m$$

and  $x_j$  and  $w_j$  are the abscissas and weights of an  $n$ -point Gauss-Laguerre integration rule and

$$k(x_j) = [k_{\beta_1}^2 + (x_j/Z)^2]^{1/2} .$$

The techniques outlined in this section are used in the computer program WESREFL which is given in Appendix B.

#### Numerical Tests

43. In the process of generating realistic seismograms, a fast Fourier transform, FFT, is used to perform the integration required by Equation 12 to convert the frequency domain representation of the solution into the desired time series. One problem that arises is the representation of a unit step function by the FFT. This arises because the FFT, unlike the Fourier transform, is periodic in time.<sup>10</sup> To avoid numerical problems associated with discontinuities, the velocity on the fault is specified rather than the displacement. This means that the seismograms computed are ground motion velocity histories rather than ground motion displacement histories. The solution, though, is amenable to either integration or differentiation to form displacement or acceleration time histories.

44. The source function used to represent the velocity of the motion of the fault is given by the function  $s(t)$ , defined as follows:

$$2\tau s(t) = \begin{cases} 0 & t \leq 0 \\ \frac{1}{2} (t/\tau)^2 & 0 \leq t \leq \tau \\ -\frac{1}{2} (t/\tau)^2 + 2(t/\tau) - 1 & \tau \leq t \leq 3\tau \\ \frac{1}{2} (t/\tau)^2 - 4(t/\tau) + 8 & 3\tau \leq t \leq 4\tau \\ 0 & t \geq 4\tau \end{cases} \quad (36)$$

The pulse  $s(t)$  is defined such that the area under the pulse is equal to one.

45. For the examples that follow the values  $\tau = 0.5, 1, 2$  sec have been used. To avoid numerical problems at high frequencies,  $s(t)$  is low pass filtered to pass frequencies less than 1.0 Hz. Figures 2 and 3 show the low pass filtered pulse and its Fourier amplitude spectrum for  $\tau = 0.5$  sec and  $\tau = 1.0$  sec, respectively. The cutoff frequency of 1.0 Hz was chosen to coincide with a spectral minimum of  $S(f)$  for  $\tau = 0.5, 1$ , or 2 sec. This choice prevents sharp discontinuities in the frequency domain, which would introduce noise in the time domain signal. This technique eliminates some of the high frequency noise problem that was present in earlier work by Herrmann and Nuttli.<sup>11,12</sup>

46. The earth model used to test the computer program WESHASK by comparison to the results of the program WESREFL is a simplified continental model (SCM) given in Table 1. This model represents a first approximation to a realistic earth model for the central United States. A second, more realistic earth model is also given in Table 1 under the heading Central United States Model (CUS). This second model is in reasonable agreement with P wave refraction and surface wave dispersion models proposed for the central United States.<sup>13,14,15,16</sup>

47. As input to the computer programs WESHASK and WESREFL,

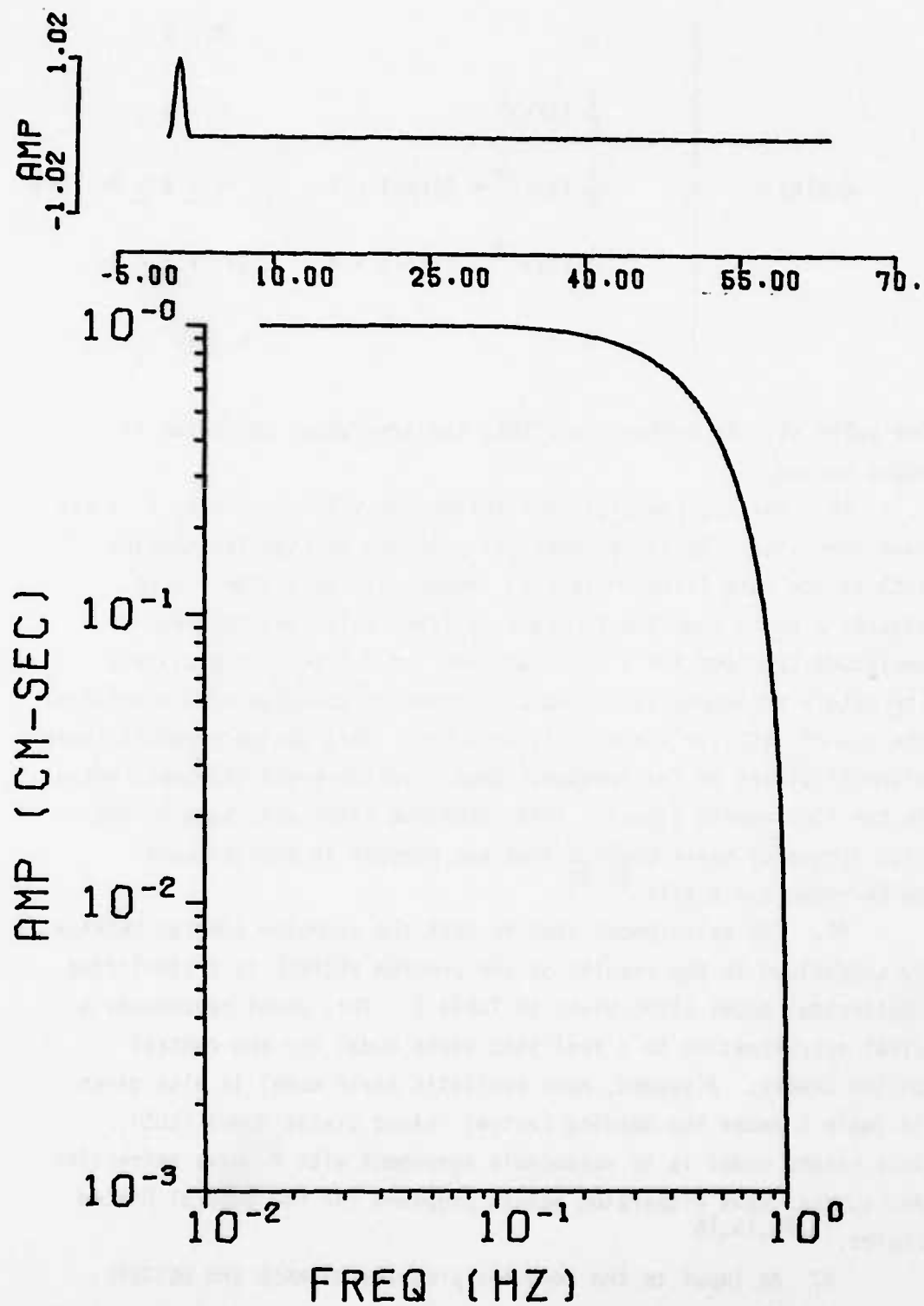


Fig. 2. Filtered source pulse and amplitude spectrum for  $\tau = 0.5$  sec.

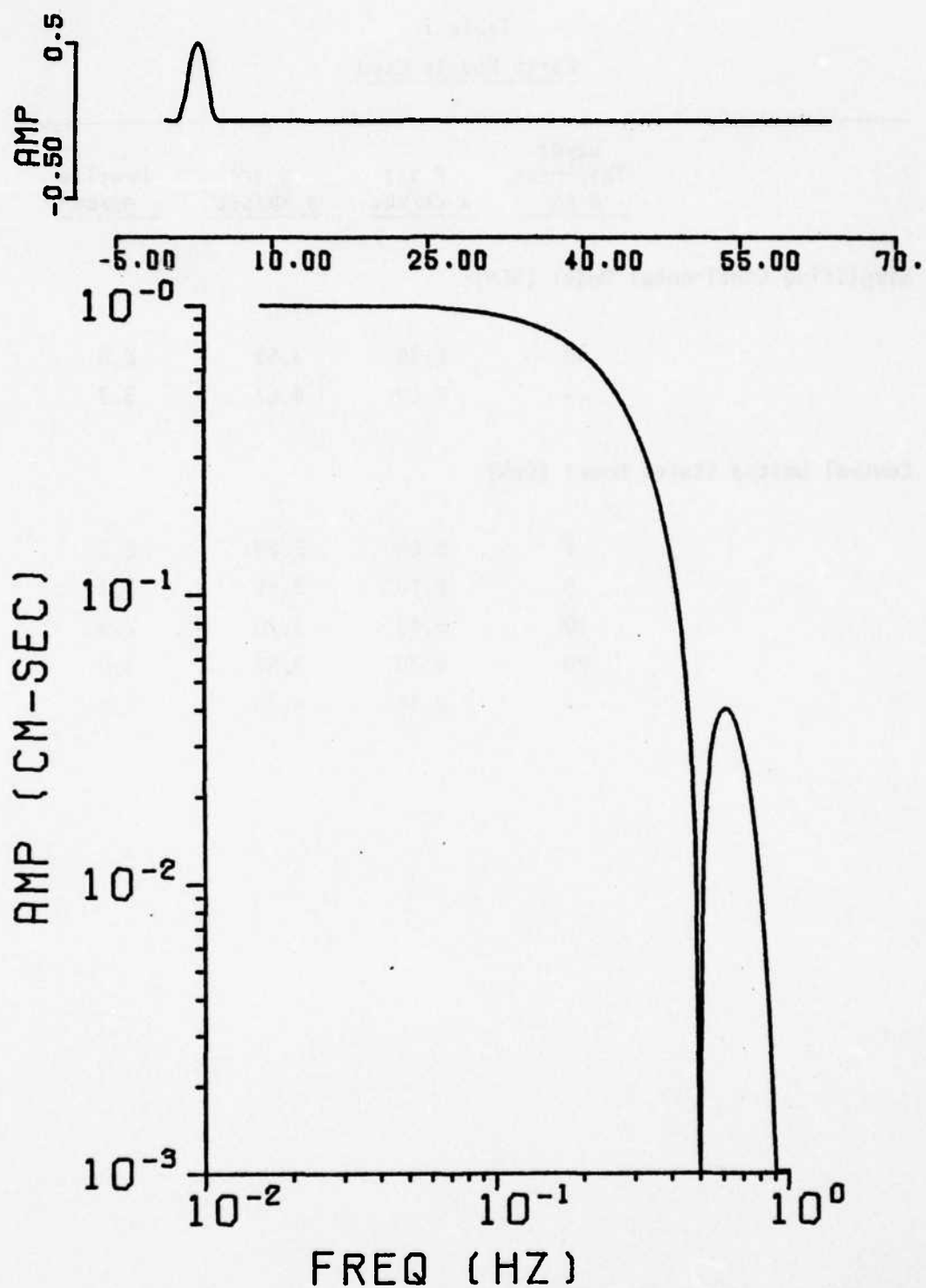


Fig. 3. Filtered source pulse and amplitude spectrum for  $\tau = 1.0$  sec.



Table 1  
Earth Models Used

<u>Layer Thickness d km</u>	<u>P Vel <math>\alpha</math> km/sec</u>	<u>S Vel <math>\beta</math> km/sec</u>	<u>Density <math>\rho</math> gm/cm<sup>3</sup></u>
Simplified Continental Model (SCM):			
40	6.15	3.55	2.8
--	8.09	4.67	3.3
Central United States Model (CUS)			
1	5.00	2.89	2.5
9	6.10	3.52	2.7
10	6.40	3.70	2.9
20	6.70	3.87	3.0
--	8.15	4.70	3.4

layer thicknesses and distances are given in units of km, the layer wave velocities are given in units of km/sec and the density is given in units of  $\text{gm/cm}^3$ . These units were chosen for ease of input of numerical data. In line with this usage, the ground motion velocity time histories are in units of cm/sec if it is understood that a source of seismic moment  $10^{20}$  dyne-cm is used. To compute the ground motion for a seismic moment of  $10^{24}$  dyne-cm, for example, one must multiply the computer output by the factor  $10^4$ . Note also that the output given is the function  $G_1$  or  $G_2$  and the results must be multiplied by the functions  $F_1$  or  $F_2$  of Equation 11 to give the proper results for comparison to real data.

48. Figure 4 is the comparison test of the  $G_1$  solution at a distance  $r = 10$  km from a source 10 km deep in the SCM model. A source with  $\tau = 1$  sec is used. To understand the relative effect and importance of each term in Equation 21, the contribution of each additional term to the final solution is shown. For ease of presentation, the time series is plotted as a function of the reduced travel time " $t - x/4.57$ " where  $t$  is the true travel time and  $x$  is the distance from the source. Figure 4a shows the pole contribution to the total solution. Figure 4b shows the effect of adding the contribution of the branch line integral along the real  $k$  axis to the pole contribution. Figure 4c shows the complete solution provided by WESHASK, e.g., that which includes the pole contribution and the contributions of the branch line integrals along the real  $k$  axis and along the negative imaginary  $k$  axis. Figure 4d is the solution provided by WESREFL. It is seen that the pole contribution is non-causal and of low amplitude. (The later arrivals are in fact early negative time arrivals because of the periodicity of the FFT). The addition of the branch line integral along the real axis improves causality and raises the signal amplitude to the final level. The branch line integral along the negative  $k$  axis affects the amplitude level only slightly while making the resultant signal causal. The agreement between the WESHASK (Figure 4c) and the WESREFL (Figure 4d) solutions is excellent. The slight motion at a reduced travel time of about 15-20 sec is due to energy reflected once from the layer boundary at a depth of 40 km.

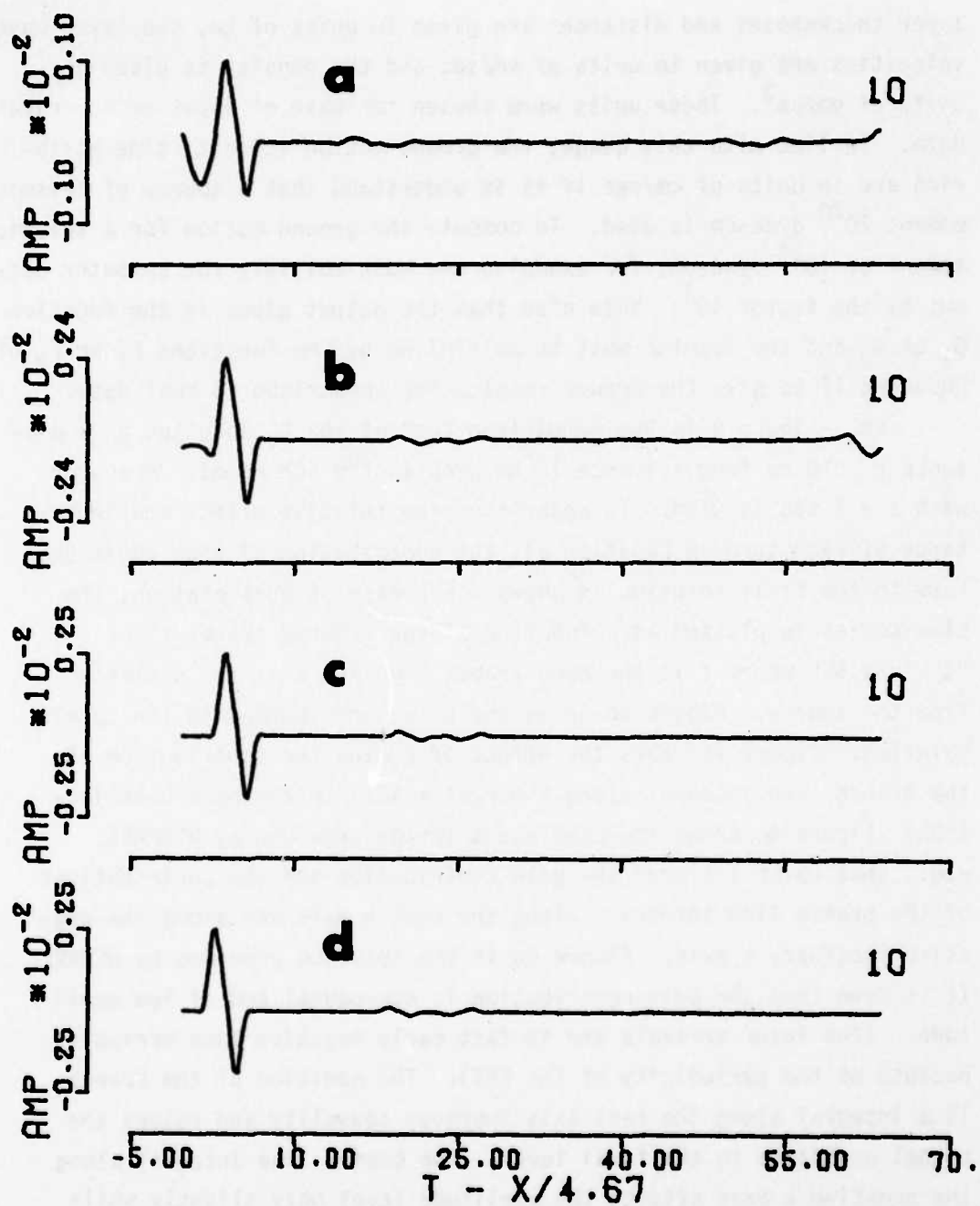


Fig. 4. a.  $G_1$  solution at 10 km, pole contribution only;  
b. Pole contribution and real axis branch line integral;  
c. Pole contribution and both branch line integrals;  
d. Ray theory solution

Figure 5 is similar to Figure 4 except that the  $G_2$  solution is shown for the same source and receiver conditions.

49. Figure 6 compares the  $G_1$  solution obtained at a distance of 300 km from the same source used to generate Figure 4. This figure shows that at large distances the pole contribution (Figure 6a) is the most important contributor to the final solution. The addition of the branch line integral along the real axis to the pole contribution (Figure 6b) makes the signal causal (e.g., no arrivals before predicted Ray theory arrivals). As expected from Equation 26, the branch line integral along the negative imaginary  $k$  axis makes an insignificant contribution at large distances because of its  $r^{-2}$  character. Again the comparison between the final solution obtained using WESHASK (Figure 6c) and the WESREFL solution (Figure 6d) is very good. Figure 7 is the  $G_2$  solution corresponding to the  $G_1$  solution of Figure 6.

50. While no independent has been developed yet to test WESHASK for more complicated earth models than a single layer overlying a half-space, it is of value to consider the importance of the various contributions of the terms of Equation 21. Figure 8 is the  $G_1$  solution for a source at a depth of 10 km in the CUS earth model. A source pulse with  $\tau = 0.5$  sec is used. From top to bottom, the various traces are the pole contribution, the contribution of the poles and real axis branch line integral, and the complete solution. As for the simple earth model at short distances, the pole contribution alone is non-causal and of low amplitude. The addition of the branch line integral along the real  $k$  axis improves causality and raises the amplitude to its final level. The addition of the branch line integral along the negative imaginary  $k$  axis makes the signal causal. Figure 9 is the  $G_2$  counterpart of Figure 8. The slight overshoot in the main pulse is an effect of only using frequencies less than 1.0 Hz.

51. Figure 10 is the  $G_1$  solution at a distance of 10 km from a source at a depth of 10 km in the CUS model. In this case a longer source pulse was used with  $\tau = 1$  sec. Figure 11 is the  $G_2$  solution corresponding to the  $G_1$  solution of Figure 10. A comparison of Figures 8-11 shows that the causality and amplitude errors

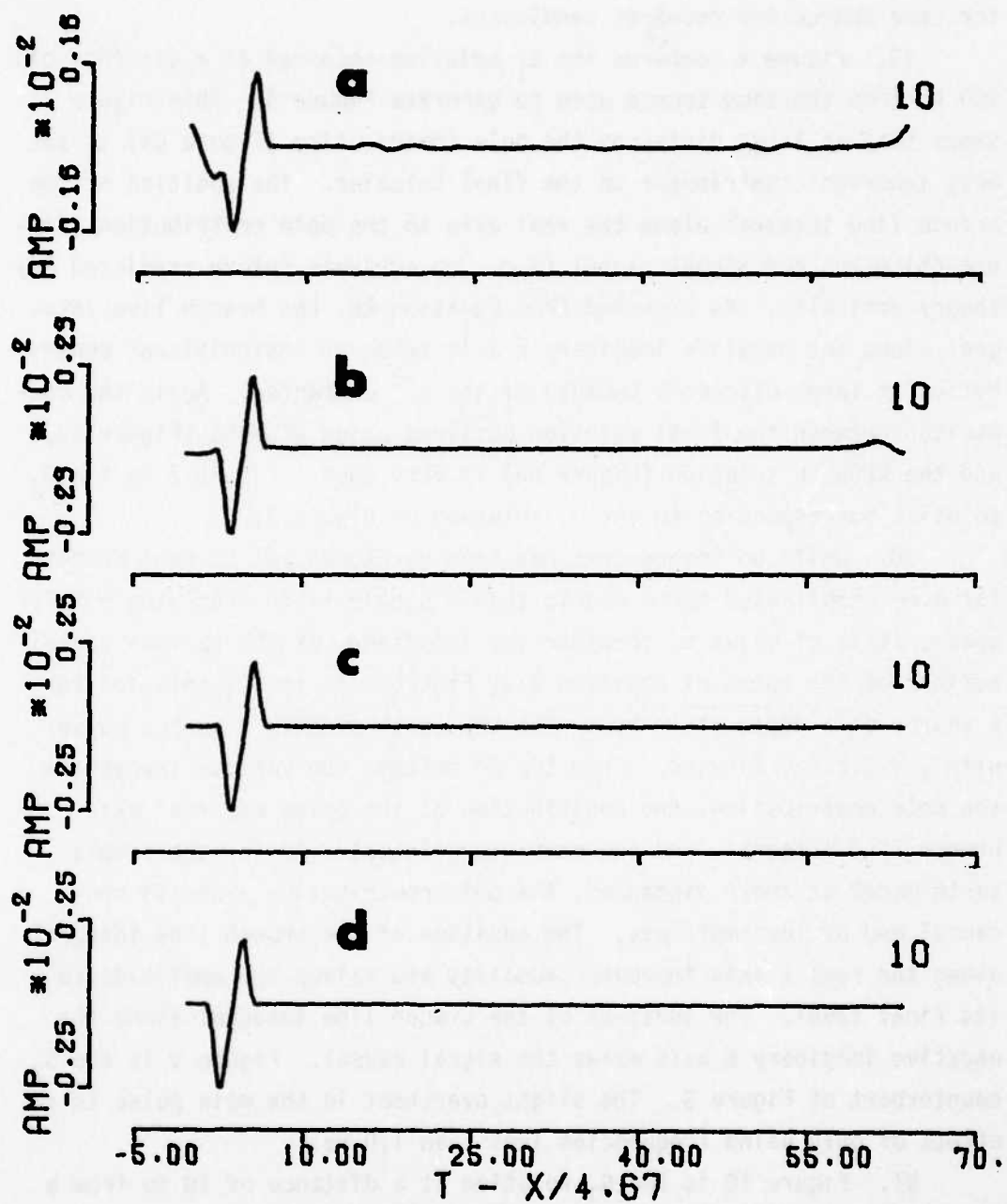


Fig. 5. a.  $G_2$  solution at 10 km, pole contribution only;  
b. Pole contribution and real axis branch line integral;  
c. Pole contribution and both branch line integrals;  
d. Ray theory solution

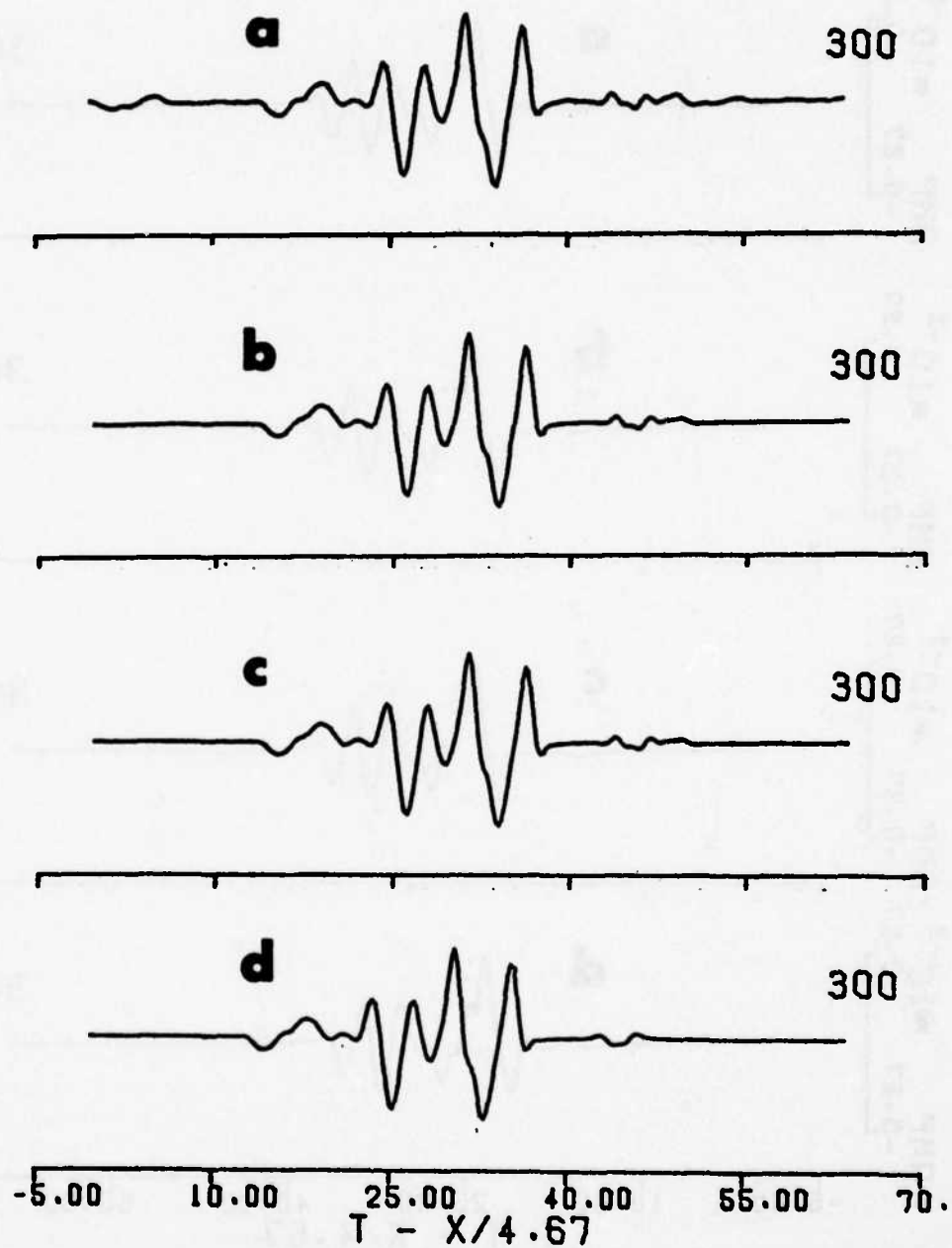


Fig. 6. a.  $G_1$  solution at 300 km, pole contribution only;  
b. Pole contribution and real axis branch line integral;  
c. Pole contribution and both branch line integrals;  
d. Ray theory solution

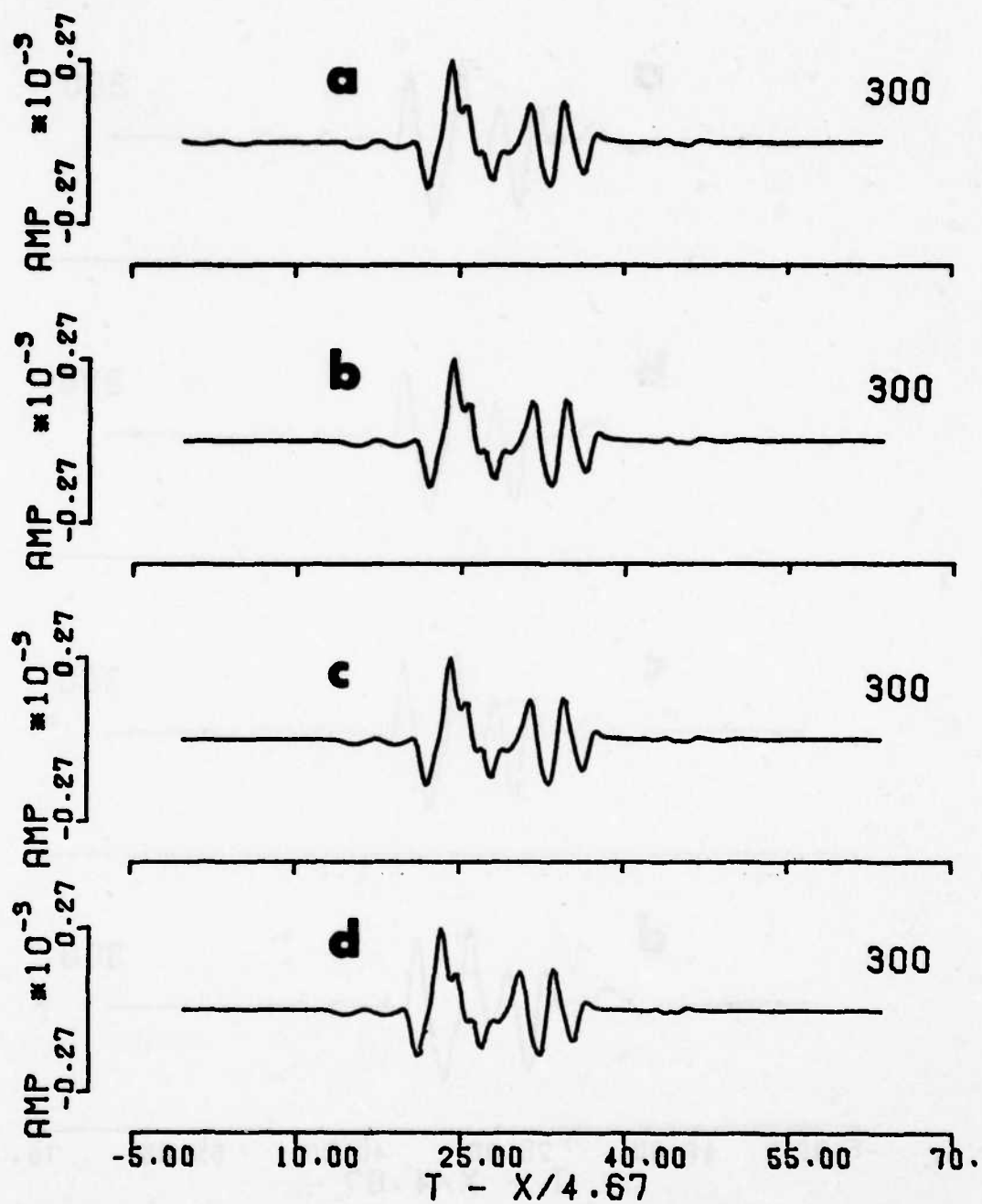


Fig. 7. a.  $G_2$  solution at 300 km, pole contribution only;  
b. Pole contribution and real axis branch line integral;  
c. Pole contribution and both branch line integrals;  
d. Ray theory solution

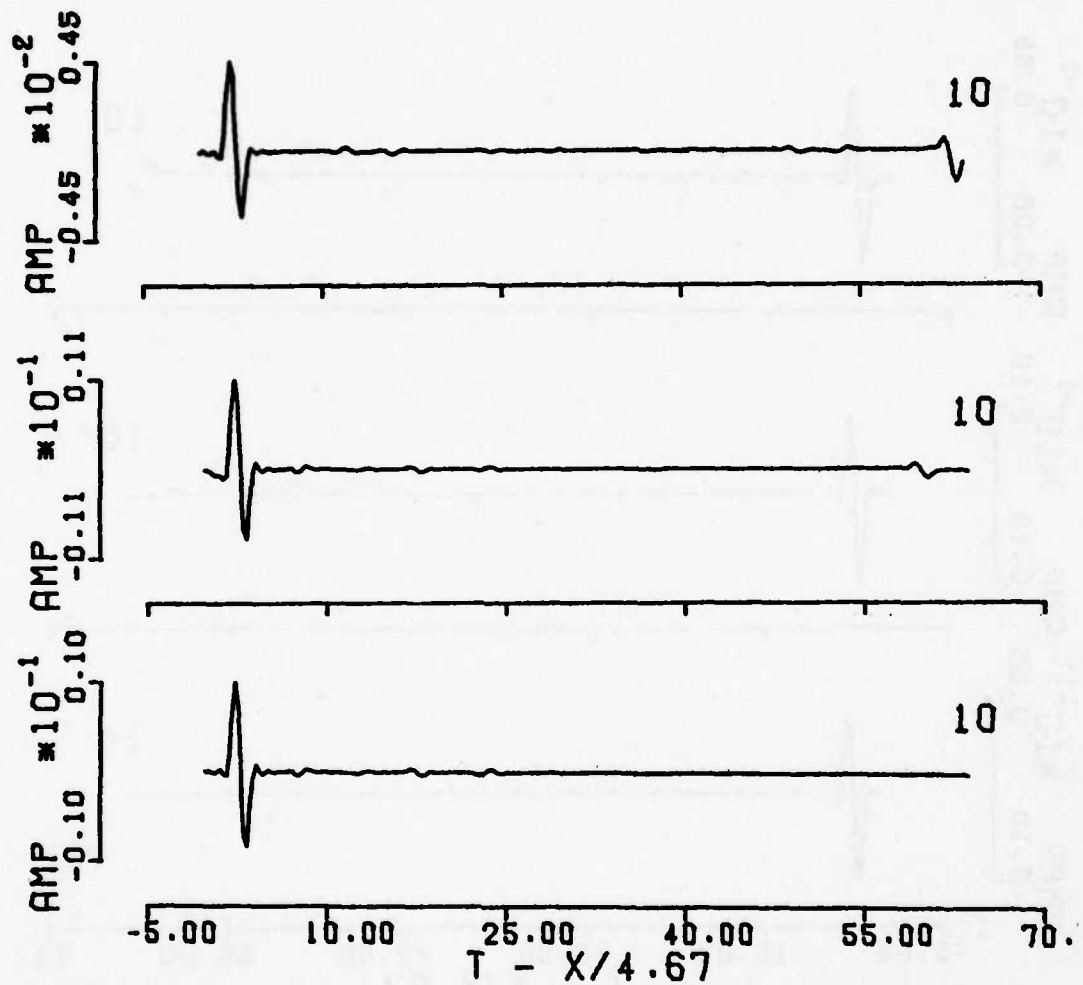


Fig. 8. Comparison of contribution to  $G_1$  for CUS model at 10 km. From top to bottom: pole contribution; pole contribution plus real axis branch line integral; complete solution.  $\tau = 0.5$  sec.



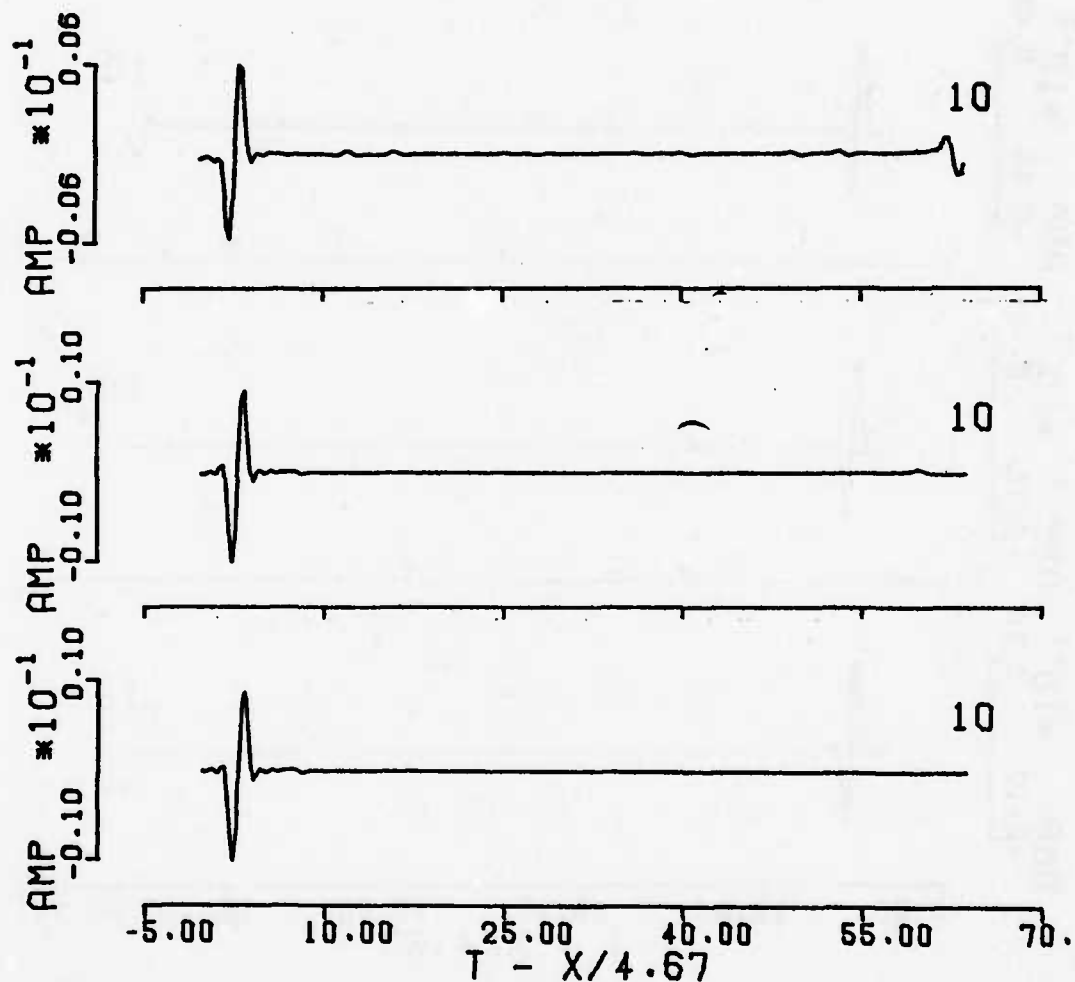


Fig. 9. Comparison of contribution to  $G_2$  for CUS model at 10 km.  
 From top to bottom: pole contribution; pole contribution  
 plus real axis branch line integral: complete solution.  
 $\tau = 0.5$  sec.

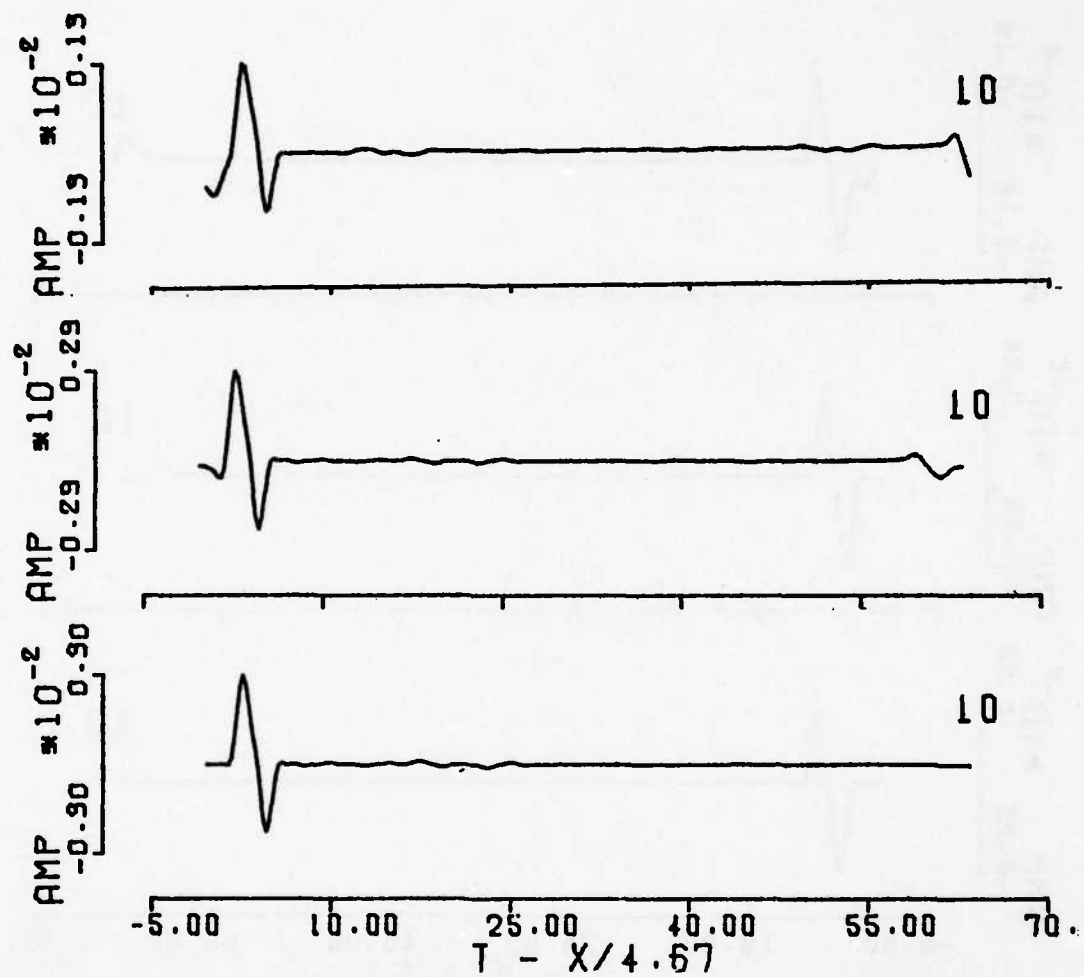


Fig. 10. Comparison of contribution to  $G_1$  for CUS model at 10 km.  
 From top to bottom: pole contribution; pole contribution  
 plus real axis branch line integral; complete solution.  
 $\tau = 1.0$  sec.

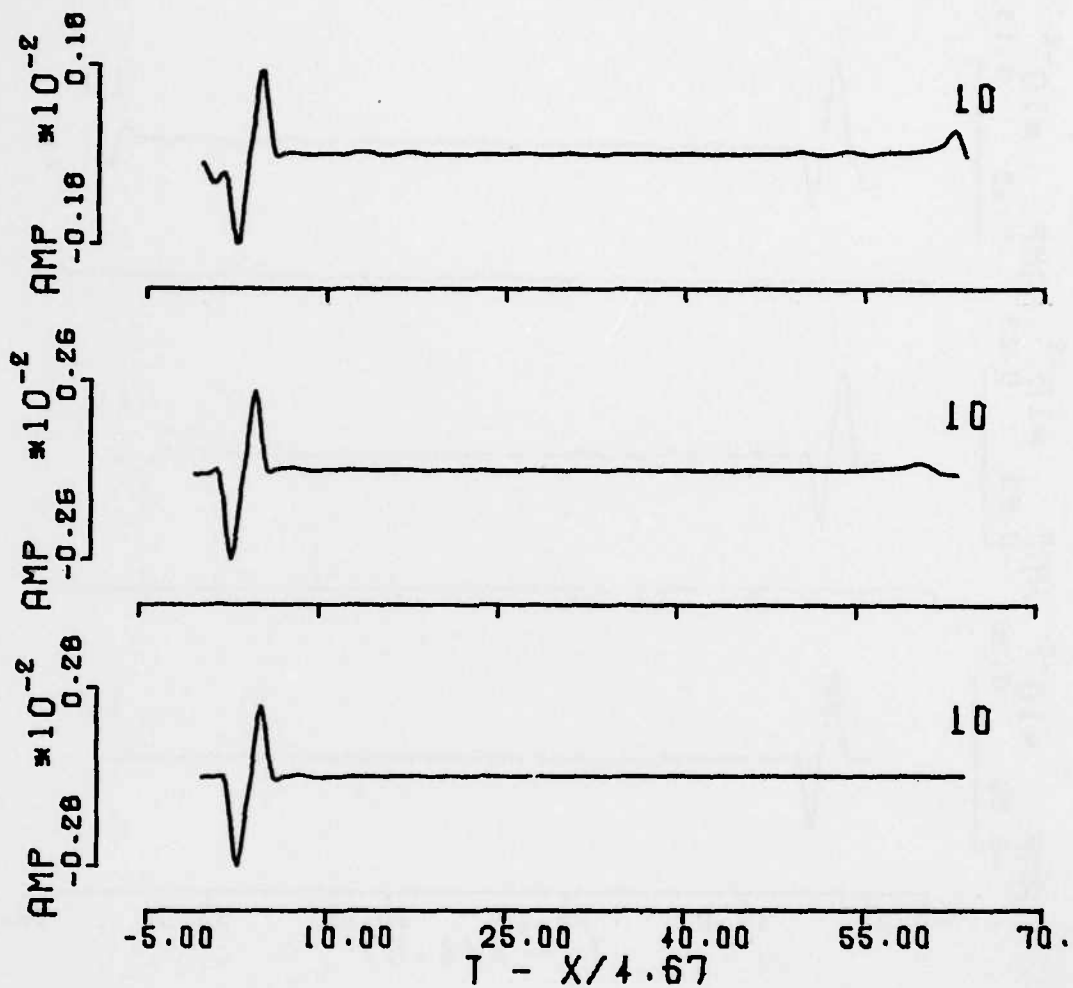


Fig. 11. Comparison of contribution to  $G_2$  for CUS model at 10 km.  
 From top to bottom: pole contribution; pole contribution  
 plus real axis branch line integral; complete solution.  
 $\tau = 1.0$  sec.

associated with using a partial solution obtained by ignoring one term of the complete expansion of Equation 21 becomes worse as a longer source pulse is used. Figures 12 and 13 are the  $G_1$  and  $G_2$  comparisons at a distance of 50 km from a source at a depth of 10 km in the CUS model with a pulse having  $\tau = 1$  sec. The pole contribution by itself yields amplitudes of the right order. The  $G_1$  solution requires the branch line integrals for causality, while the  $G_2$  solution is almost completely described by the pole contribution alone.

52. The value of the exercise just performed by studying the solutions shown in Figures 8 - 13, is that distance ranges at which computational efficiency can be obtained are indicated. For example, at short distances, the complete solution complete with poles and branch line integrals must be obtained. At large distances, especially, if one is not interested in causality, the pole contribution by itself suffices to provide a very realistic estimate of the final solution. By not having to perform the branch line integral along the negative imaginary axis at distances greater than 100 km, for example, considerable computer time can be saved in obtaining the final solution.

53. Figure 14 shows the dependence of  $G_1$ , left side, and  $G_2$ , right side, upon distance. The source is at a depth of 10 km in the SCM model. A source pulse with  $\tau = 1$  sec is used. Secondary arrivals due to deep reflections are very prominent in the  $G_1$  solution since the vertical dip slip source is very efficient at generating waves that leave the source in a near vertical direction. On the other hand the vertical strike slip source or  $45^\circ$  dip slip source is not very efficient at generating near vertical waves. Hence, the near vertical reflections are more prominent in the  $G_1$  solution. At larger distances, rays which left the source near vertically at short distances reflect off the interface at the depth of 40 km with angles near the critical angle. As a ray becomes supercritically reflected, there is little energy loss upon reflection and a phase change is introduced. It is seen from Figure 14 that very low amplitude phases at short distances become large contributors to the signal

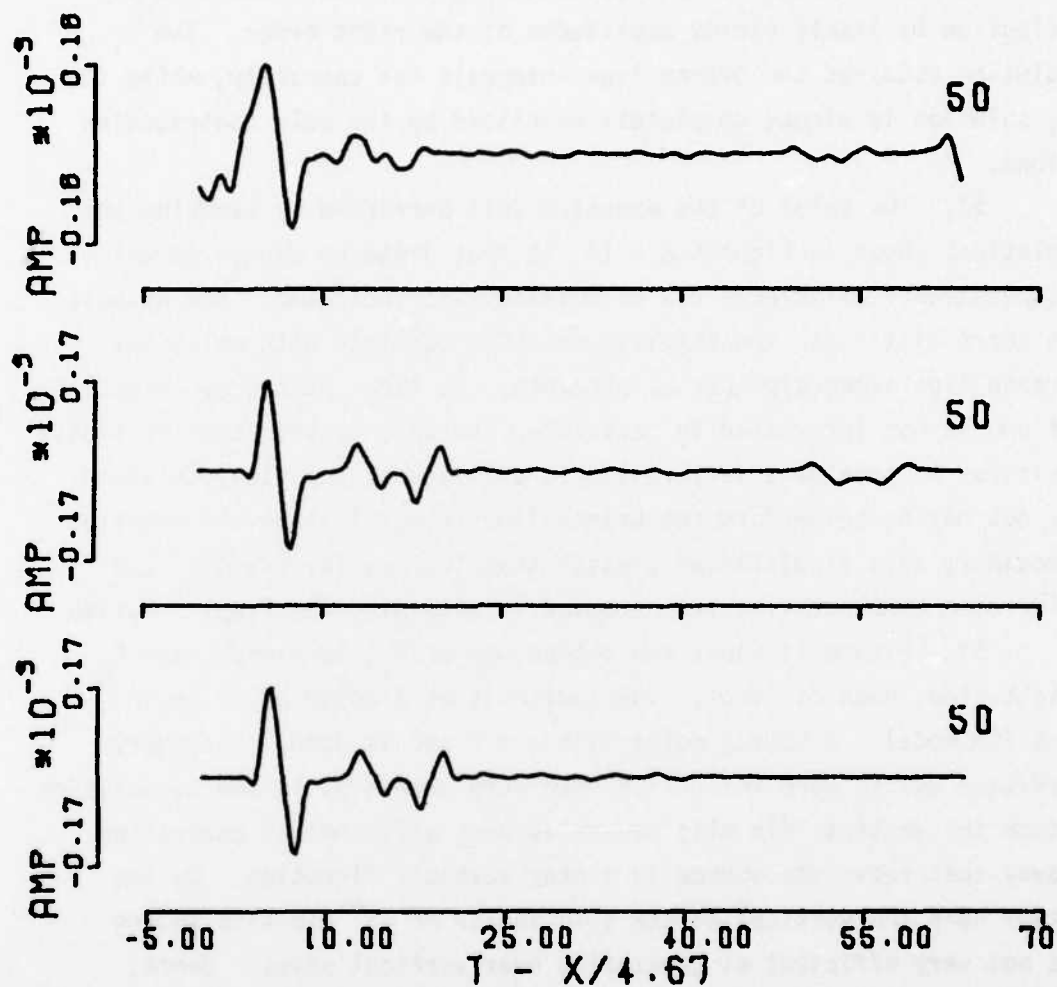


Fig. 12. Comparison of contribution to  $G_1$  for CUS model at 50 km.  
 From top to bottom: pole contribution, pole contribution  
 plus real axis branch line integral; complete solution.  
 $\tau = 1.0$  sec.

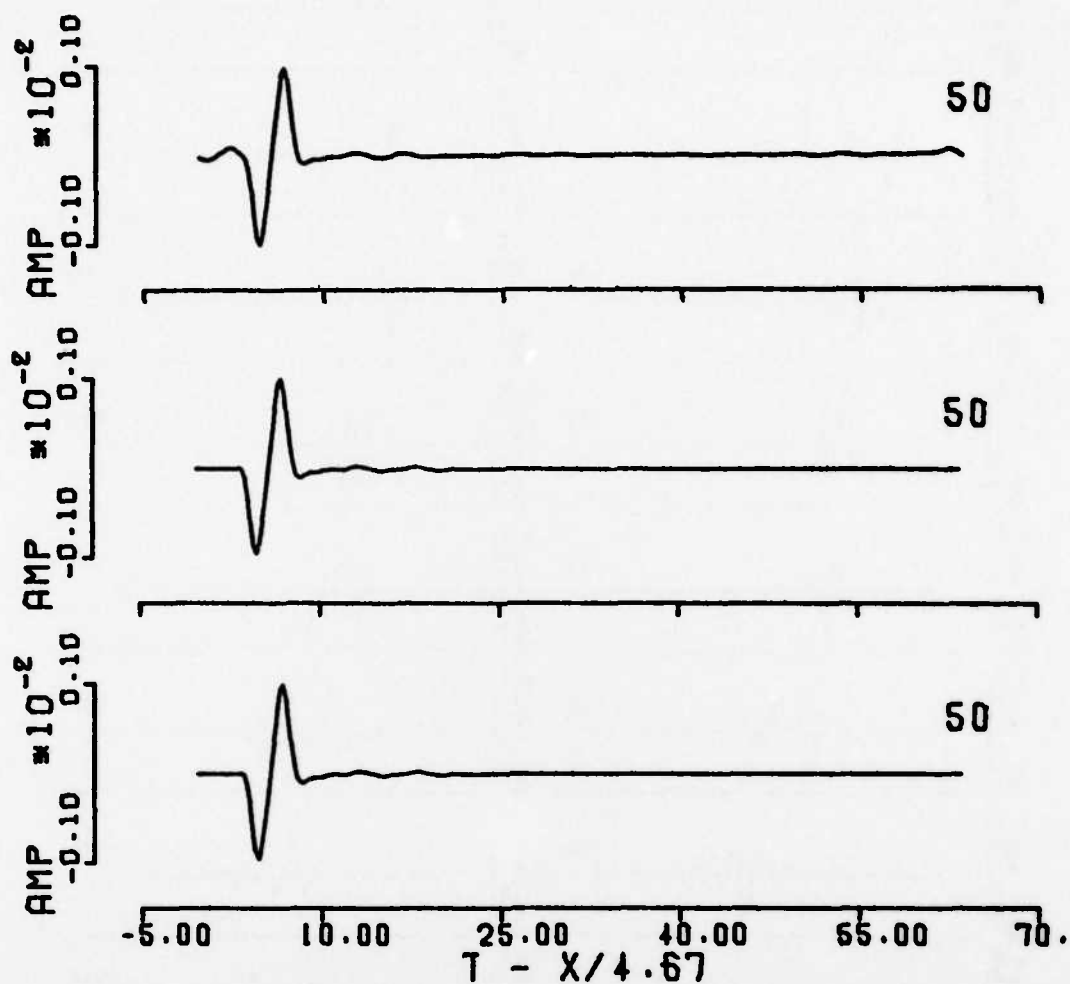


Fig. 13. Comparison of contribution to  $G_2$  for CUS model at 50 km.  
 From top to bottom: pole contribution; pole contribution  
 plus real axis branch line integral; complete solution.  
 $\tau = 1.0$  sec.

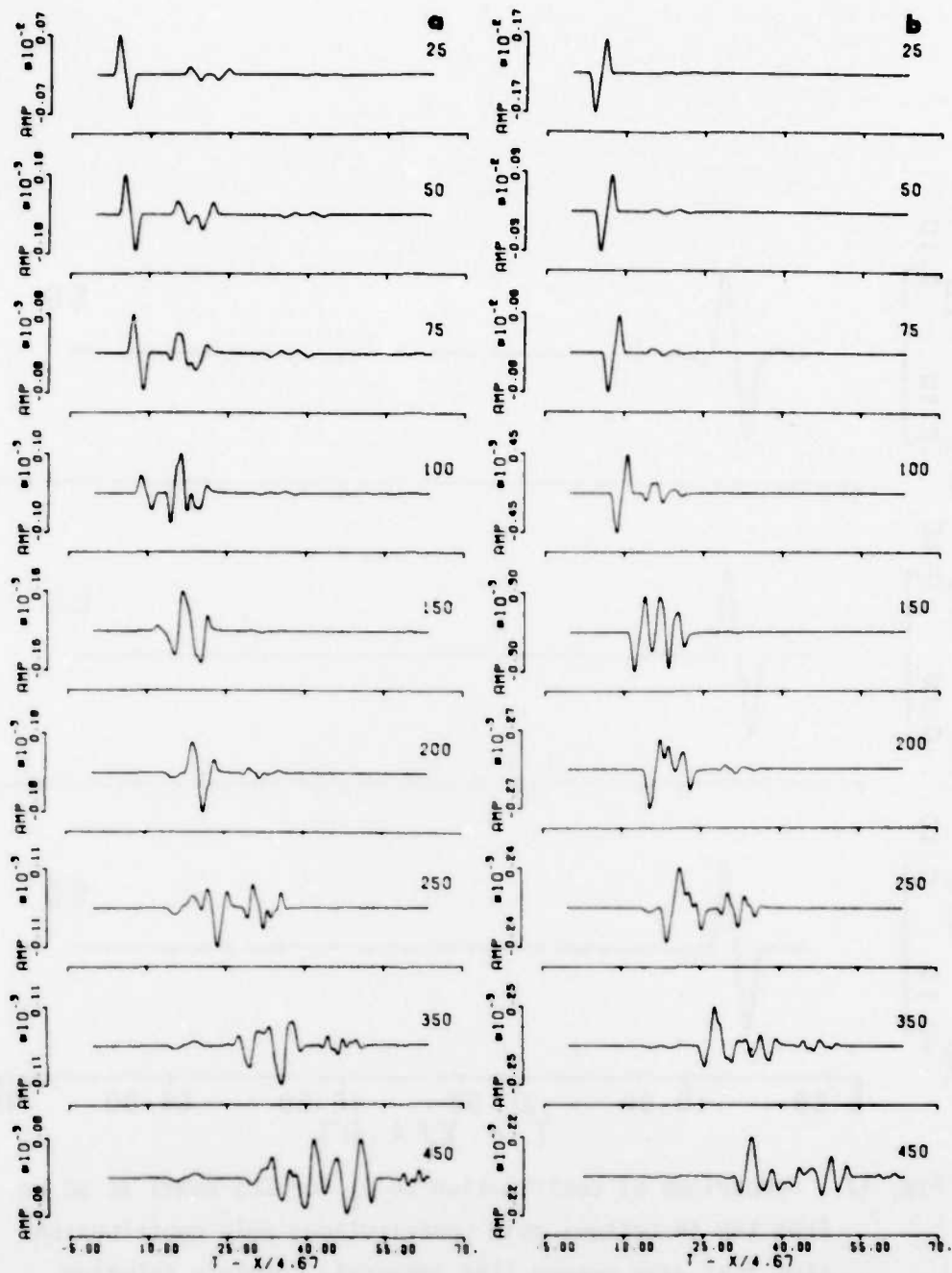


Fig. 14. Comparison of  $G_1$  solution, a, and  $G_2$  solution, b, for SCM model as a function of distance in km from a source at depth of 10 km with  $\tau = 1.0$  sec.

at large distances for precisely this reason. It is also seen how the various multiple reflections combine together to form what is known as a surface wave at large distances. The refraction arrival is of relatively small amplitude compared to the surface wave at large distances. The progression of the SH wave signal from a simple pulse at short distances to the surface wave, called Love wave, is gradual. The surface wave can be said to take over from the direct pulse at a distance at which the first supercritically reflected waves arrive. At this point the waveform changes from a simple pulse to a complicated set of arrivals.

54. Figure 15 compares the  $G_1$  and  $G_2$  solutions as a function of distance for a source with  $\tau = 1.0$  sec at a depth of 10 km in the CUS earth model. There seems to be very little difference between this solution and that presented in Figure 14 at short distances. However, at large distances, the arrivals are no longer as distinct because the more complicated earth model permits many more reflections and refractions by the various layers. Figure 16 shows the  $G_1$  and  $G_2$  solutions as a function of distance for a source with  $\tau = 0.5$  sec at a depth of 10 km in the CUS earth model. With the shorter source pulse the various crustal reflections can be easily seen compared to Figure 15 with the longer source pulse. A close examination of the records indicates that numerical noise is present only at the very short and very large distances, as is expected from the discussion of numerical integration techniques used.



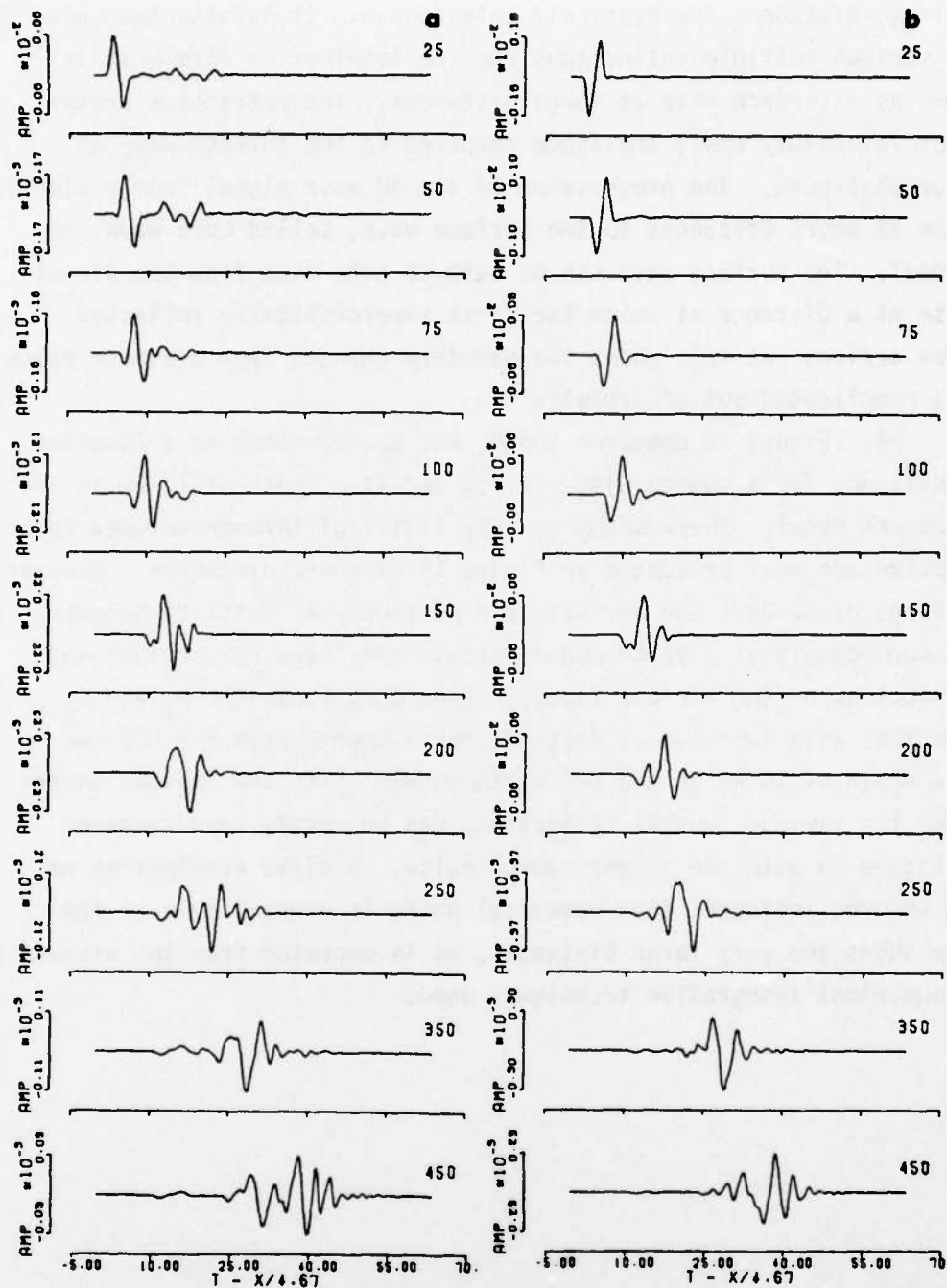


Fig. 15. Comparison of  $G_1$  solution, a, and  $G_2$  solution, b, for CUS model as a function of distance in km from a source at a depth of 10 km with  $\tau = 1.0$  sec

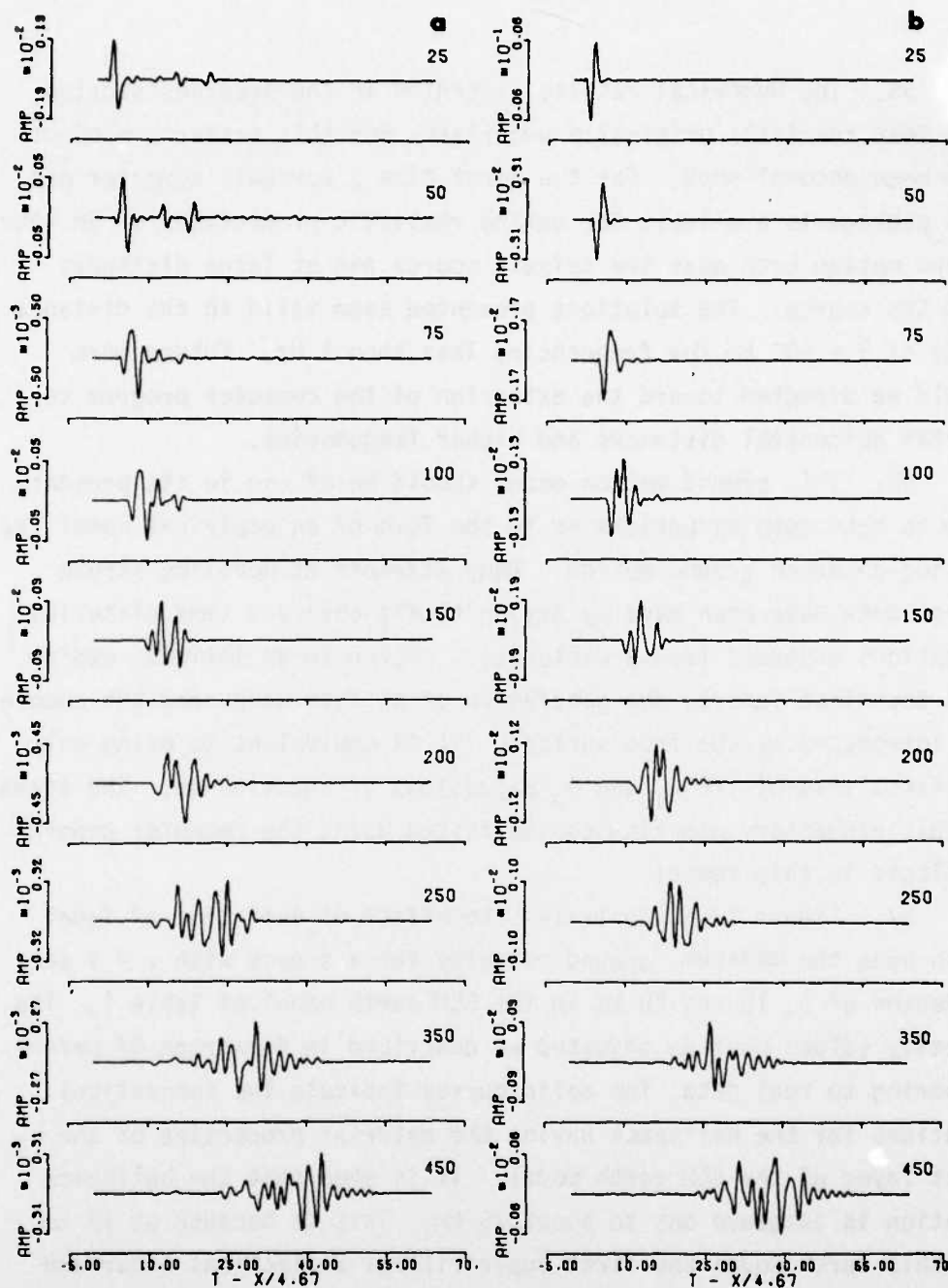


Fig. 16. Comparison of  $G_1$  solution, a, and  $G_2$  solution, b, for CUS model as a function of distance in km from a source at a depth of 10 km with  $\tau = 0.5$  sec

#### PART IV: SUMMARY AND CONCLUSIONS

55. The numerical results presented in the previous section show that the tasks originally undertaken for this research project have been accomplished. For the first time a workable computer program package is available for making realistic predictions of SH wave ground motion both near the seismic source and at large distances from the source. The solutions presented seem valid in the distance range of 5 - 500 km for frequencies less than 1 Hz. Future work should be directed toward the extension of the computer program to shorter epicentral distances and higher frequencies.

56. This ground motion model should be of use in its present form to make some deductions as to the form of an empirical model for fitting observed ground motion. Many attempts at modeling strong motion data have been made by trying to fit observed time histories to motions expected from a dislocation source in an infinite medium.<sup>17</sup> This technique ignores the generation of surface waves and the complexity introduced by the free surface. It is equivalent to using only the first term of the  $G_1$  and  $G_2$  expansions of Equation 28. The adequacy of this elementary modeling can be tested using the computer programs developed in this report.

57. Figure 17 demonstrates the effect of variation of focal depth upon the maximum ground velocity for a source with  $\tau = 1$  sec at depths of 5, 10 and 20 km in the SCM earth model of Table 1. The velocity values must be adjusted as described in Paragraph 47 before comparing to real data. The solid curves indicate the theoretical solutions for the halfspace having the material properties of the first layer of the SCM earth model. It is seen that the halfspace solution is adequate out to about 75 km. This is because at 75 km for this earth model the first supercritical reflections occur and the surface wave begins to form. The difference in the geometrical spreading between the  $G_1$  and  $G_2$  solutions is due to the difference in radiation patterns between the two basic solutions. Figure 18

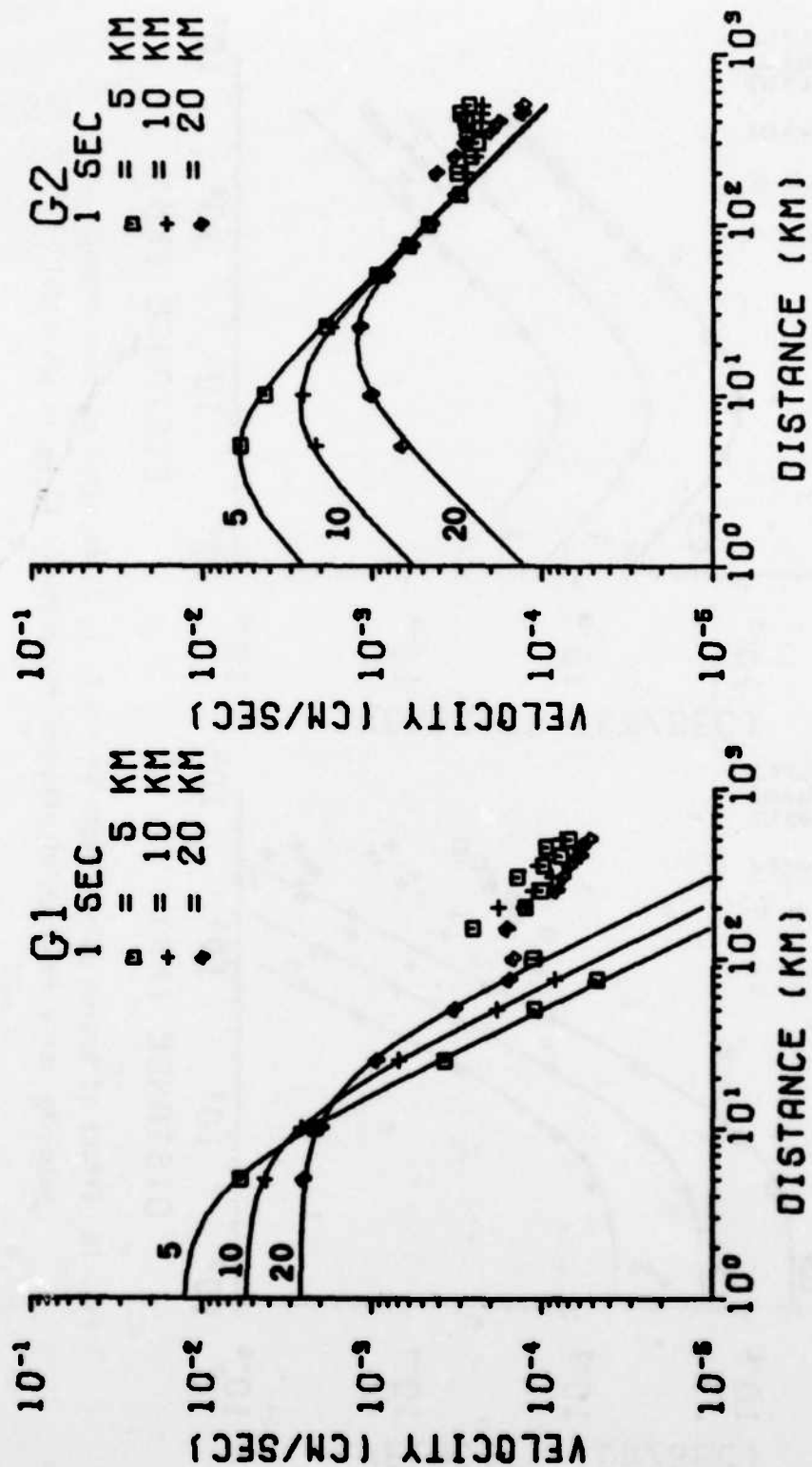


Fig. 17. Effect of focal depth variation (5, 10, 20 km) upon maximum ground  
as a function of distance for  $\tau = 1.0$  sec  
using SCM model

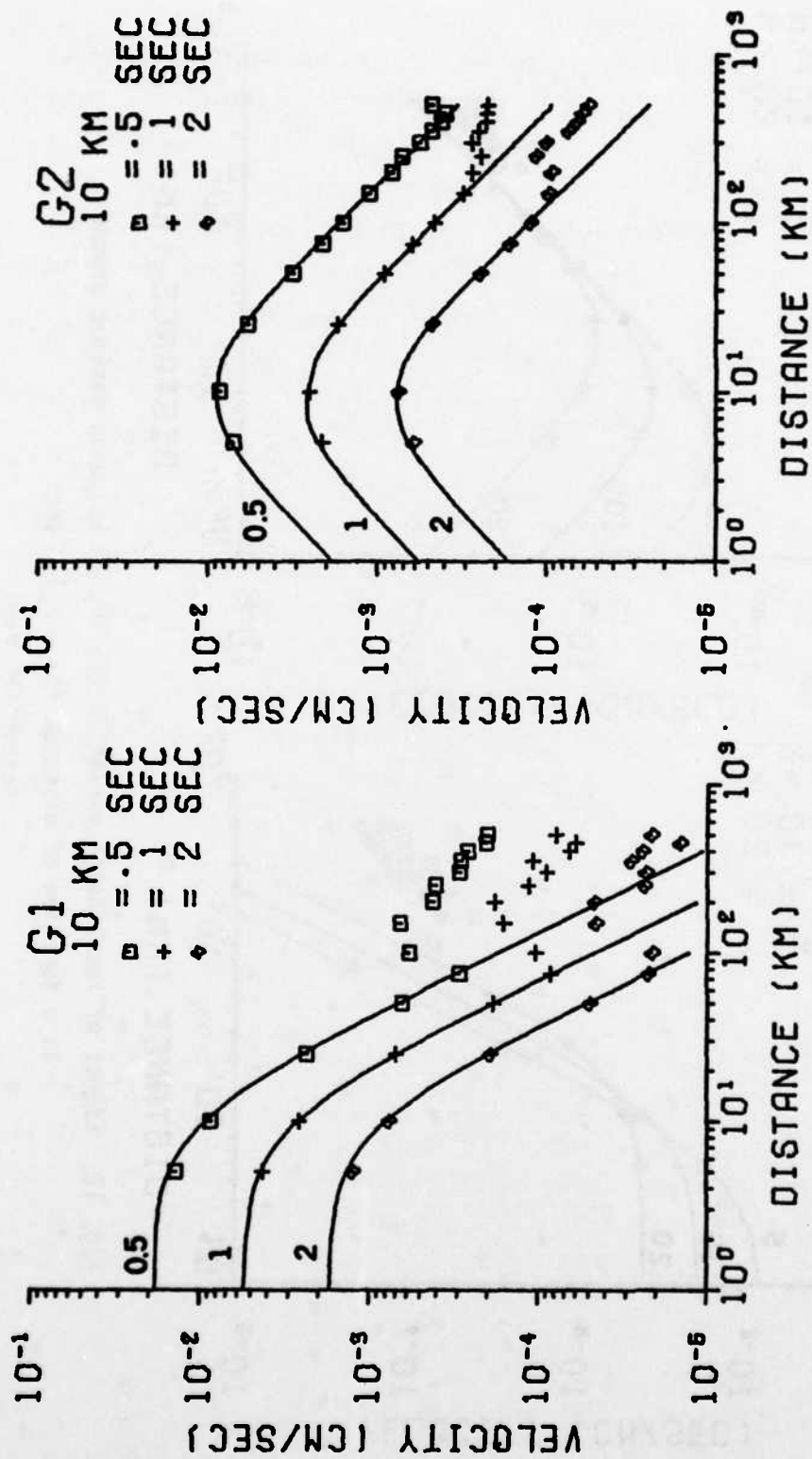


Fig. 18. Effect of source pulse length ( $\tau = 0.5, 1, 2$  sec) upon maximum ground velocity as a function of distance for depth of 10 km in SCM model

shows the effect of variation of source pulse length for a source at a depth of 10 km in the SCM earth model. The maximum ground velocity was computed using  $\tau = 0.5, 1$  and 2 sec. For a constant area under the source pulse, or in other terms a constant seismic moment, the maximum ground velocity increases as  $\tau$  decreases. The effect of the transition from a pulselike arrival to a surface wave is again seen at a distance of 75 km by the departure of the computed solution for the SCM earth model indicated by the symbols and the halfspace approximation given by the solid lines.

58. Figures 17 and 18 were obtained for a very simple earth model. The computer program WESHASK can be used to do a similar study for other earth models and source parameters. For a crustal model with a shallower depth to the crust-mantle interface, simple model scaling indicates that the transition from a near-field pulselike ground motion character to a far-field surface wave character would occur at shorter epicentral distances than for the SCM earth model. It is quite feasible to determine figures similar to Figures 17 and 18 for a southern California earth model in order to obtain an insight as to the empirical shape to use when fitting southern California strong motion data as a function of distance.

59. Aside from giving an insight into the nature of gross ground motion parameter modeling, such as maximum velocity versus distance, the computer program developed here should be able to predict strong motion ground displacement time histories for real earthquakes as well as the generalized ray technique of Helmberger and Malone.<sup>1</sup> To predict strong motion acceleration time histories, whose high frequency content is strongly affected by the heterogeneities of the real earth, further research is required on the statistical modeling of high frequency waves scattered from these heterogeneities. When this is done, a technique proposed by Herrmann<sup>18</sup> could be used to yield a synthetic seismogram having the coherent low frequency character described by the theory presented in this report and the high frequency content of the scattered waves. Such a ground motion time history would be as realistic as is presently possible.



## REFERENCES

1. HelMBERGER, D. V. and Malone, S. D., "Modeling Local Earthquakes as Shear Dislocations in a Layered Half Space," Journal of Geophysical Research, Vol 80, No. 35, 1975, pp 4381-4888.
2. HelMBERGER, D. V., "Generalized Ray Theory for Shear Dislocations," Bulletin, Seismological Society of America, Vol 64, No. 1, 1974, pp 45-64.
3. Vered, M., and Ben-Menahem, A., "Application of Synthetic Seismograms to the Study of Low-Magnitude Earthquakes and Crustal Structure in the Northern Red Sea Region," Bulletin, Seismological Society of America, Vol 64, No. 4, 1974, pp 1221-1237.
4. Haskell, N. A., "Radiation Pattern of Surface Waves from Point Sources in a Multi-Layered Medium," Bulletin, Seismological Society of America, Vol 54, No. 1, 1964, pp 377-393.
5. Hudson, J. A., "A Quantitative Evaluation of Seismic Signals at Teleseismic Distances--II. Body Waves and Surface Waves from an Extended Source," Geophysical Journal, Royal Astronomical Society, Vol 18, No. 4, 1969, pp 353-370.
6. Harkrider, D. G., "Potentials and Displacements for Two Theoretical Seismic Sources," Geophysical Journal, Royal Astronomical Society, Vol 47, No. 1, 1976, pp 97-133.
7. Herrmann, R. B., "A Student's Guide to the Use of P and S Wave Data for Focal Mechanism Determination," Earthquake Notes, Eastern Section, Seismological Society of America, Vol 46, No. 4, 1975, pp 29-39.
8. Ewing, W. M., Jardetzky, W. S., and Press, F., Elastic Waves in Layered Media, McGraw-Hill, New York, 1957.
9. Stroud, A. H., and Secrest, D. H., Gaussian Quadrature Formulas, Prentice-Hall, Englewood Cliffs, 1966.
10. Brigham, E. O., The Fast Fourier Transform, Prentice-Hall, Englewood Cliffs, 1974.
11. Herrmann, R. B., and Nuttli, O. W., "Ground-Motion Modelling at Regional Distances for Earthquakes in a Continental Interior, I. Theory and Observations," Earthquake Engineering and Structural Dynamics, Vol 4, No. 1, 1975, pp 49-58.
12. Herrmann, R. B., and Nuttli, O. W., "Ground-Motion Modelling at Regional Distances for Earthquakes in a Continental Interior, II.

Effect of Focal Depth, Azimuth and Attenuation," Earthquake Engineering and Structural Dynamics, Vol 4, No. 1, 1975, pp 59-72.

13. McEvilly, T. V., "Central U. S. Crust-Upper Mantle Structure from Love and Rayleigh Wave Phase Velocity Inversion," Bulletin, Seismological Society of America, Vol 54, No. 6, 1964, pp 1997-2015.
14. Stewart, S. W., "Crustal Structure in Missouri by Seismic Refraction Methods," Bulletin, Seismological Society of America, Vol 58, No. 1, 1968, pp 291-323.
15. Nuttli, O. W., Stauder, W., and Kisslinger, C., "Travel-Time Tables for Earthquakes in the Central United States," Earthquake Notes, Eastern Section, Seismological Society of America, Vol XL, No. 4, 1969, pp 19-28.
16. Stauder, W., Dowling, J., and Jackson, W. H., "The Billiken Calibration Shot," Scientific Report No. AFCRL-64-659, Bedford, Air Force Cambridge Research Laboratories, 1964.
17. Trifunac, M. D., "A Three-Dimensional Dislocation Model for the San Fernando, California, Earthquake of February 9, 1971," Bulletin, Seismological Society of America, Vol 64, No. 1, 1974, pp 149-172.
18. Herrmann, R. B., "A Method for Synthesis of the Seismic Coda of Local Earthquakes," J. Geophys (in press), 1977.



In accordance with letter from DAEN-RDC, DAEN-ASI dated 22 July 1977, Subject: Facsimile Catalog Cards for Laboratory Technical Publications, a facsimile catalog card in Library of Congress MARC format is reproduced below.

Herrmann, Robert B

Earthquake generated SH waves in the near field and near-regional field / by Robert B. Herrmann, St. Louis University, Department of Earth and Atmospheric Sciences, St. Louis, Missouri. Vicksburg, Miss. : U. S. Waterways Experiment Station, 1977.

51, 25, 18 p. : ill. ; 27 cm. (Miscellaneous paper - U. S. Army Engineer Waterways Experiment Station ; S-77-12)

Prepared for Office, Chief of Engineers, U. S. Army, Washington, D. C., under Contract DACW 39-76-C-0058.

References: p. 50-51.

1. Earthquake prediction. 2. Ground motion predictions. 3. Seismic waves. 4. Shear waves. 5. Wave propagation. I. United States. Army. Corps of Engineers. II. St. Louis University. Dept. of Earth and Atmospheric Sciences. III. Series: United States. Waterways Experiment Station, Vicksburg, Miss. Miscellaneous paper ; S-77-12. TA7.W34m no.S-77-12.

